



Kinematic Structure of the Galactic Center S Cluster

Basel Ali¹ , Daria Paul¹, Andreas Eckart^{1,2} , Marzieh Parsa^{1,2}, Michal Zajacek^{2,3} , Florian Peißker¹ , Matthias Subroweit¹,
 Monica Valencia-S.¹, Lauritz Thomkins¹, and Gunther Witzel²

¹ I. Physikalisches Institut der Universität zu Köln, Zùlpicher Str. 77, D-50937 Köln, Germany; eckart@ph1.uni-koeln.de

² Max-Planck-Institut für Radioastronomie, Auf dem Hügel 69, D-53121 Bonn, Germany

³ Center for Theoretical Physics, Polish Academy of Sciences, Al. Lotnikow 32/46, 02-668 Warsaw, Poland
 Received 2019 December 30; revised 2020 March 31; accepted 2020 April 21; published 2020 June 17

Abstract

We present a detailed analysis of the kinematics of 112 stars that mostly comprise the high-velocity S cluster and orbit the supermassive black hole Sgr A* at the center of the Milky Way. For 39 of them, orbital elements are known; for the remainder, we know proper motions. The distribution of the inclinations and the proper motion flight directions deviate significantly from a uniform distribution, which one expects if the orientation of the orbits are random. Across the central arcseconds, the S-cluster stars are arranged in two almost edge-on disks that are located at a position angle approximately $\pm 45^\circ$ with respect to the Galactic plane. The angular momentum vectors for stars in each disk point in both directions, i.e., the stars in a given disk rotate in opposite ways. The poles of this structure are located only about 25° from the line of sight. This structure may be the result of a resonance process that started with the formation of the young B-dwarf stars in the cluster about 6 Myr ago. Alternatively, it indicated the presence of a disturber at a distance from the center comparable to the distance of the compact stellar association IRS 13.

Unified Astronomy Thesaurus concepts: Galactic center (565); Black holes (162); Star clusters (1567); Stellar dynamics (1596)

Supporting material: animation, machine-readable tables

1. Introduction

The Galactic Center (GC) stellar cluster harbors a number of stellar associations with different ages and potentially different origins. The luminous $20\text{--}30M_\odot$ O/WR stars appear to reside in at least one single disk-like structure most likely coupled to their formation process (Levin & Beloborodov 2003; Yelda et al. 2014). Their ages have been derived as 6 ± 2 Myr (Paumard et al. 2006). The S cluster, consisting of lighter $3.5\text{--}20 M_\odot$ stars, contains the 4 million solar-mass supermassive black hole (SMBH, Sgr A*; Parsa et al. 2017; Gravity Collaboration et al. 2018) and appears to be somewhat decoupled from the stellar disk at larger radii. Of $K_s \leq 18$ stars that reside with separations of less than $1''$ or those stars that have known semimajor axes of less than $1''$, the predominant fraction are B stars. This is especially true for the brightest of the stars (Gillessen et al. 2017; Habibi et al. 2017).

Gillessen et al. (2009) also derive the volume density distribution of the the S-cluster B stars. They find for the 15 stars with a semimajor axes of less than $0.5''$ in projection a three-dimensional power-law slope of -1.1 ± 0.3 . This appears to be marginally larger than the slope derived for a more spread out cluster population of B stars, implying that the S stars form a distinct possibly cusp-like component.

A detailed near-infrared spectroscopic study of the S stars (Ghez et al. 2003; Martins et al. 2008; Habibi et al. 2017) shows that these stars are most likely high-surface-gravity (dwarf) stars. The authors' analysis reveals an effective temperature of $21,000\text{--}28,500$ K, a rotational velocity of $60\text{--}170 \text{ km s}^{-1}$, and a surface gravity of $\log g = 4.1\text{--}4.2$. These properties are characteristic for stars of spectral-type B0-B3V with masses between $8 M_\odot$ and $14 M_\odot$. Their age is estimated to be less than 15 Myr. For the early B-dwarf

(B0–B2.5V) star S2 (Martins et al. 2008), the age is estimated to be $6.6^{+3.4}_{-4.7}$ Myr. This compares well with the age of the clockwise-rotating disk (CWD) of young stars in the GC. Habibi et al. (2017) conclude that the low ages for the high-velocity stars favor a scenario in which they formed in a local disk rather than in field binaries subjected to binary disruption and stellar scattering.

The stars in galactic bulges or central stellar clusters often show peculiar kinematic arrangements. From theory (e.g., Contopoulos 1988), observations of external galaxies, and the Milky Way (MW), it has become evident that boxy and peanut-shape stellar orbits have a significant influence on the appearance of galactic bulges. Perturbations in the vertical direction lead to orbits with a boxy appearance (Chaves-Velasquez et al. 2017). Hernquist & Weinberg (1992) also described boxy and disk-like appearances as possible structures in post-merger bulges. Quillen et al. (1997) discovered boxy and peanut-shape bulges in highly inclined galaxies. Quillen et al. (2014) present a simple resonant Hamiltonian model for the vertical response of a stellar disk to the growth of a bar perturbation. As the perturbation grows, the stars become trapped in vertical inner Lindblad resonances and are lifted into higher-amplitude orbits. The vertical structure of a boxy and peanut-shape bulge as a function of radius and azimuthal angle in the galaxy plane can be predicted from the strength and speed of the bar perturbation and the derivatives of the gravitational potential. This model predicts that stars on the outer side of the resonance are lifted higher than stars on the inner side, offering an explanation for the sharp outer edge of the box/peanut.

The MW is a barred galaxy whose central bulge has a box/peanut shape and consists of multiple stellar populations with different orbit distributions (e.g., Gerhard et al. 2016). Infrared observations revealed that the MW bulge shows a boxy/peanut

or X-shaped bulge. Simulations indicate that about 20% of the mass of the MW bar is associated with the shape (Abbott et al. 2017).

While these structures are associated with resonances linked to a bar or central cluster potential, they can also be the result of a perturbation due to interacting mass. Gualandris & Merritt (2009) study the short- and long-term effects of an intermediate-mass black hole (IMBH) on the orbits of stars bound to the SMBH at the center of the MW. The authors consider 19 stars in the S-star cluster and an SMBH mass between 400 and 4000 M_\odot and a distance from Sgr A* between 0.3 and 30 mpc. They find that for the more massive perturbers, the orbital elements of the S stars could experience changes at the level of about 1% in just a few years. On timescales of 1 Myr or longer, the IMBH efficiently randomizes the eccentricities and orbital inclinations of the S stars. These results support, on the one hand, that the relatively short-scale response of the S stars to a nearby perturbation can occur. On the other hand, the orbits are clearly not fully randomized, implying that a recent perturbation by massive IMBH within the S cluster can be excluded. Resonances could occur, however, if a perturber is located outside the S cluster.

In Section 2, we present the observations and data reduction. In the discussion in Section 3, we first show in Section 3.1 the histograms and visualizations that highlight our observational results. In Section 3.2, we discuss our findings in terms of stellar dynamical considerations. A summary and conclusions are given in Section 4. Finally, in Section 5, we describe the three enhanced graphics that show the projected orbital arrangements in motion.

2. Observations and Data Reduction

The positions of the S stars are calculated from the AO-assisted imaging data of the GC from 2002–2015 taken by the NAOS-CONICA (NACO) instrument installed at the fourth (from 2001–2013) and then the first (from 2014 on) unit telescope of the Very Large Telescope (VLT).⁴ The K_s -band (2.18 μm) images obtained by the S13 camera (with a 13 mas pix^{-1} scale) and the S27 camera of NACO (with a 27 mas pix^{-1} scale) are used. The AO guide star is IRS 7 with $K_s = 6.5\text{--}7.0$ mag located at about $5''.5$ north of Sgr A*. The data reduction consists of the standard steps like flat-fielding, sky subtraction, and bad-pixel correction. A cross-correlation algorithm is used to align the dithered exposures. We use the 27 mas pix^{-1} scale images to measure the position of the SiO maser stars IRS 9, IRS 10EE, IRS 12N, IRS 15NE, IRS 17, IRS 19NW, IRS 28, and SiO-15 (Menten et al. 1997; Reid et al. 2003, 2007), which were needed to find the connection of the NACO NIR data and the radio reference frame. In order to measure the position of the S stars, the Lucy–Richardson deconvolution algorithm is used to resolve the sources in the 13 mas pix^{-1} scale images. For each epoch, we included all available K_s -band frames of the GC stellar cluster that were taken with a close to diffraction-limited AO correction and showed Sgr A* flaring. We use the reduced data presented by

Table 1
Parameters for the Disk Solutions

i_b	R'	R/R'	μ	ΔR
90	1	3.00	3.0	0.15
90	3.5	1.30	4.0	0.070
90	6.2	1.13	6.6	0.042
90	10.4	1.05	10.7	0.018
0	1	0.77	3.0	0.13
0	3.5	0.90	4.0	0.070
0	7.2	0.97	7.5	0.033
0	11.1	0.98	11.4	0.018

Note. Listed are i_b , the inclination of the stellar disks to the orbit of the perturber; R' , the initial ratio of the semimajor axes of the stars in the disk and the perturber; R/R' , the current ratio of the stellar disk in relation to the initial ratio; μ , the value of Tisserand’s parameter that is expected to be preserved; and ΔR , half the variation width of the current ratio of semimajor axes.

Witzel et al. (2012), Table 2, 2003 to mid-2010, and Eckart et al. (2013), Table 1, and Shahzamanian et al. (2015), Table 1, 2002–2012. We supplemented additional imaging data for observing epochs in 2016, 2017, and 2018 for all sources and further 2019 data for the sources S62, S29, S19, S42, S38, S60. For the stars S2 and S38, we also used the positions published by Boehle et al. (2016) for the years 1995–2010 and 2004–2013, respectively. As described by Parsa et al. (2017; and following the approach by Gillessen et al. 2009), the data were added by applying a constant linear positional shift between the two data sets. In addition, we took into account the mean difference between the proper motions of the VLT and Keck coordinate systems. These differences become evident, e.g., in Table 1 in Gillessen et al. (2017; see also Boehle et al. 2016).

The selected objects comprise all stars brighter than $K_s = 18.0$ that are detectable at all epochs and show no signs of being severely confused with other stars of the cluster for most epochs (see also the discussion by Sabha et al. 2012; Eckart et al. 2013). An overview image is shown in Figure 1. The positional results were verified by using stars S7, S10, S26, S30, and S65 as references as these object have almost straight flight paths with no detectable curvature. For the stars with orbital sections that are short or show no curvature, we fitted a straight line to the flight path.

Plewa et al. (2015) find from the average velocity differences in radial and tangential directions that the infrared reference frame shows neither pumping nor rotation relative to the radio system to within $\sim 7.0 \mu\text{as yr}^{-1} \text{ arcsec}^{-1}$. Over 20 yr, this amounts to an upper limit of about $0''.14$, i.e., typically to 0.1–0.2 mas across the central $1''$ diameter cluster of high-velocity stars. Hence, verifying the positional measurements using stars with straight flight paths leaves us with an uncertainty of less than 0.5 mas for the 13 mas pix^{-1} scale images.

In addition to the positional measurements that substantially cover sections of the curved orbits as made use of the time variable radial velocities and their uncertainties as presented in Figure 8 by Gillessen et al. (2017).⁵ This includes the radial velocity data for S2 from the AO-assisted field spectrometer SINFONI installed on the fourth unit telescope of the VLT and

⁴ Program IDs: 60.A-9026(A), 713-0078(A), 073.B-0775(A), 073.B-0085(E), 073.B-0085(F), 077.B-0552(A), 273.B-5023(C), 073.B-0085(I), 077.B-0014(C), 077.B-0014(D), 077.B-0014(F), 078.B-0136(A), 179.B-0261(A), 179.B-0261(H), 179.B-0261(L), 179.B-0261(M), 179.B-0261(T), 179.B-0261(N), 179.B-0261(U), 178.B-0261(W), 183.B-0100(G), 183.B-0100(D), 183.B-0100(I), 183.B-0100(J), 183.B-0100(T), 183.B-0100(U), 183.B-0100(V), 087.B-0017(A), 089.B-0145(A), 091.B-0183(A), 095.B-0003(A), 081.B-0648(A), 091.B-0172(A).

⁵ This covers S1, S2, S4, S8, S9, S12, S13, S14, S17, S18, S19, S21, S24, S31, S38, and S54.

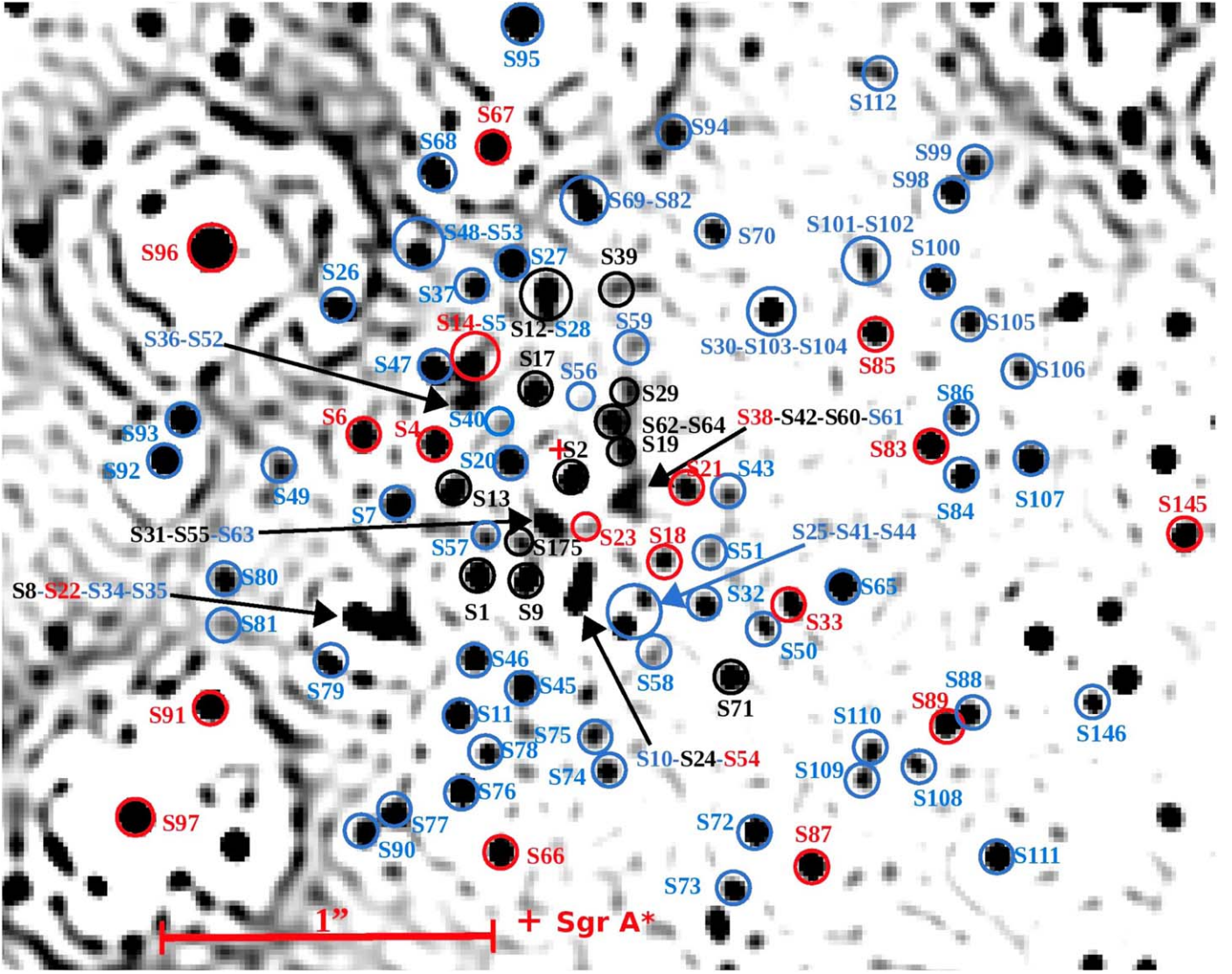


Figure 1. Map of the region showing the S cluster and some neighboring stars. East is to the left, north is up. We included their nomenclature and encircled two or three stars if they happen to be close together at the epoch of the image. The image was obtained by NACO at the VLT in early 2018. Sgr A*, the counterpart of the supermassive black hole, is located at the position of the red cross. Stars encircled by red and black lines belong to the corresponding disk systems described in Section 3. For all of these stars, orbital elements are known. Blue circles mark the stars for which we only have short linear sections of their orbits.

taken from Gillessen et al. (2009). The radial velocity measurements used for S38 are from Boehle et al. (2016).

For the central stars that have larger orbital sections measured, we modeled the Newtonian stellar orbits by integrating the equation of motion using the fourth-order Runge–Kutta method with 12 or 6 initial parameters, respectively (i.e., the positions and velocities in three dimensions). To determine the six orbital elements, a corresponding number of observables must be provided. These are the projected positions α , δ ; the proper motions v_α , v_δ ; the radial velocity v_z ; and the projected orbital acceleration. However, higher order moments of the latter two quantities can also be used as replacements or in support. The results compare favorably with those of the fitting routine starting by solving Kepler’s equation, which can be done using the iterative Newtonian method. This optimization method is implemented in Python in the Scipy package under the name Sequential Least Squares Programming. The optimized results along with boundaries on each of the elements are then used for bootstrap resampling to get error estimations. We used a fixed

central black hole mass of $4.3 \times 10^6 M_\odot$ at a distance of 8.3 kpc (Gillessen et al. 2017; Parsa et al. 2017). The results are listed in the appended Tables 2 and 3.

However, we point out that ambiguities in the inclinations of the orbits due to missing radial velocity information do not affect our prime observables as used in Section 3.1.3. These are the directions of the semimajor axes of the sky-projected orbits and the projected true (i.e., three-dimensional) semimajor axes of the orbits. These quantities are listed in Tables 4 and 5. In total, we analyzed 105 S-cluster members and seven sources (S66, S67, S83, S87, S91, S96, S97) that belong to the the clockwise-rotating stellar disk (CWD) of He stars (Levin & Beloborodov 2003; Paumard et al. 2006). This results in our case in 39 stars with orbital elements; for the remaining stars, we fitted straight trajectories. These compare well within the uncertainties with the parameters derived for 40 stars by Gillessen et al. (2017). For a discussion of the organization of S-cluster sources, see also Yelda et al. (2014). For the remaining stars, we just fit a straight line to obtain their proper

Table 2
Orbital Elements for Stars in the Black Disk

Star	a (mpc)	Δa (mpc)	e	Δe	i (deg)	Δi (deg)	ω (deg)	$\Delta \omega$ (deg)	Ω (deg)	$\Delta \Omega$ (deg)	t_{clos} (yr)	Δt_{clos} (yr)
1.	2.	3.	4.	5.	6.	7.	8.	9.	10.	11.	12.	13.
S1	22.675	0.257	0.665	0.003	121.066	0.401	109.893	0.458	352.484	0.286	2000.261	0.001
S2	5.034	0.001	0.887	0.002	137.514	0.401	73.416	0.745	235.634	1.031	2002.390	0.020
S8	16.637	0.182	0.768	0.022	75.057	0.573	337.931	2.120	317.075	0.630	1979.216	0.037
S9	11.125	0.030	0.791	0.036	81.876	0.458	137.854	0.573	158.079	0.229	1972.924	0.023
S12	11.962	0.105	0.906	0.003	33.060	0.516	311.173	0.802	236.173	1.146	1995.881	0.001
S13	9.580	1.264	0.415	0.030	24.694	7.219	256.513	11.459	47.842	15.126	2004.015	0.507
S17	13.037	0.794	0.421	0.020	95.799	0.172	319.481	3.495	194.118	1.432	1991.906	0.067
S19	11.122	3.130	0.626	0.090	72.021	2.807	131.093	12.261	337.415	4.469	2004.275	0.004
S24	45.115	7.475	0.682	0.061	95.226	4.240	244.596	3.151	14.381	1.604	2023.963	0.311
S29	34.694	3.803	0.335	0.078	100.955	0.688	331.341	11.975	171.257	1.432	2054.568	4.322
S31	16.582	4.514	0.521	0.151	108.919	10.256	321.487	24.603	145.990	19.882	2019.201	1.132
S39	13.919	2.068	0.831	0.042	86.058	13.002	36.784	9.339	159.282	0.688	1999.108	0.338
S42	38.562	4.057	0.644	0.043	67.666	0.802	37.930	2.578	206.379	1.031	2011.876	0.716
S55	4.360	0.002	0.740	0.010	141.692	1.604	133.499	3.896	129.890	4.183	2009.310	0.030
S60	20.369	1.799	0.832	0.033	130.806	2.979	42.743	11.688	193.774	17.189	2021.883	1.103
S62	3.603	0.002	0.980	0.000	61.765	0.057	45.034	0.057	112.414	0.057	2003.441	0.009
S64	15.952	3.947	0.347	0.161	113.789	2.406	154.985	31.883	165.699	7.047	2005.906	6.192
S71	39.052	1.266	0.916	0.043	67.151	4.354	336.842	2.120	35.466	2.578	1689.433	18.447
S175	29.808	0.001	0.999	0.001	93.793	0.001	65.260	0.001	349.733	0.001	2009.976	0.001

Note. Following the stellar designation in column (1), we list consecutively the following quantities with their uncertainties: semimajor axis, ellipticity, inclination, argument of periaipse, longitude of ascending node, and the time of closest approach.

(This table is available in machine-readable form.)

Table 3
Orbital Elements for Stars in the Red Disk

Star	a	Δa	e	Δe	i	Δi	ω	$\Delta \omega$	Ω	$\Delta \Omega$	t_{clos}	Δt_{clos}
	(mpc)	(mpc)			(deg)	(deg)	(deg)	(deg)	(deg)	(deg)	(yr)	(yr)
1.	2.	3.	4.	5.	6.	7.	8.	9.	10.	11.	12.	13.
S4	14.555	0.034	0.443	0.014	80.386	0.229	286.823	0.229	259.092	0.229	1954.476	0.011
S6	25.229	0.574	0.891	0.021	86.459	1.490	119.175	0.974	86.116	3.782	1932.803	5.140
S14	9.037	2.426	0.798	0.287	107.716	21.944	378.668	28.904	231.532	19.194	2000.453	3.942
S18	9.253	0.212	0.461	0.017	111.727	4.011	374.084	3.724	54.202	1.833	1997.061	0.006
S21	8.662	0.162	0.772	0.016	59.530	1.891	161.173	3.266	262.930	0.917	2027.290	0.017
S22	52.357	2.553	0.489	0.062	106.914	0.859	94.366	15.756	289.859	3.953	1996.959	5.234
S23	10.389	1.945	0.462	0.205	47.326	6.303	30.882	13.980	249.638	26.986	2024.577	8.064
S33	31.326	4.263	0.664	0.059	64.057	1.891	304.183	2.464	107.086	4.412	1923.847	11.286
S38	5.598	0.205	0.812	0.050	157.774	15.011	11.001	9.626	96.375	8.308	2003.406	0.339
S54	48.225	10.890	0.897	0.018	58.384	2.120	151.891	4.641	254.164	5.672	2002.326	0.042
S66	61.777	2.985	0.160	0.028	126.738	1.432	144.271	7.850	87.892	2.292	1794.519	13.396
S67	47.708	1.938	0.082	0.045	131.895	2.292	226.548	4.469	79.756	5.042	1740.000	15.852
S83	58.717	4.729	0.377	0.048	125.592	1.261	207.697	7.391	87.433	7.506	2049.789	14.833
S85	184.115	3.611	0.773	0.006	85.084	1.089	157.907	4.183	107.544	0.974	1930.384	8.658
S87	109.645	1.066	0.163	0.060	117.514	1.662	334.779	3.610	105.367	2.578	627.690	12.927
S89	42.801	2.027	0.651	0.224	91.731	1.490	123.644	1.089	234.282	1.547	1777.211	21.179
S91	78.892	1.958	0.322	0.034	113.560	2.005	366.120	4.870	101.643	2.636	1086.879	21.025
S96	54.529	1.070	0.289	0.078	127.712	2.865	238.179	5.730	121.582	4.927	1688.413	22.780
S97	92.859	2.783	0.382	0.033	112.300	1.891	38.503	4.354	109.148	2.177	2161.556	14.970
S145	42.278	0.501	0.550	0.016	83.136	7.506	177.388	2.406	263.904	0.229	1808.606	4.260

Note. Following the stellar designation in column (1), we list consecutively the following quantities with their uncertainties: semimajor axis, ellipticity, inclination, argument of periaipse, longitude of ascending node, and the time of closest approach.

(This table is available in machine-readable form.)

Table 4
Position Angles of the Black Disk

Star	$m1(t, \text{R.A.})$ (mas yr ⁻¹)	$\Delta m1$ (mas yr ⁻¹)	$m2(t, \text{decl.})$ (mas yr ⁻¹)	$\Delta m2$ (mas yr ⁻¹)	Φ (deg)	$\Delta\Phi$ (deg)
1.	2.	3.	4.	5.	6.	7.
S1	0.767	0.086	8.710	0.086	5.035	0.562
S2	1.608	0.951	-21.019	0.951	175.624	2.584
S8	-14.616	0.233	14.989	0.233	-44.278	0.637
S9	-10.771	0.472	22.951	0.472	-25.141	1.066
S12	4.253	0.292	17.785	0.292	13.450	0.914
S13	0.678	0.334	-17.274	0.334	177.751	1.108
S17	-5.771	0.319	-22.271	0.319	-165.473	0.795
S19	-5.404	0.241	12.290	0.241	-23.735	1.030
S24	2.820	0.068	13.475	0.068	11.820	0.284
S29	-1.500	0.054	10.578	0.054	-8.070	0.289
S31	-6.491	0.159	12.484	0.159	-27.471	0.646
S39	4.367	0.195	-12.792	0.195	161.153	0.826
S42	7.952	0.076	13.161	0.076	31.141	0.282
S55	-4.814	1.328	28.810	1.328	-9.487	2.605
S60	-2.209	0.163	16.687	0.163	-7.542	0.556
S62	15.992	1.793	-20.849	1.793	142.511	3.910
S64	3.155	0.173	-15.407	0.173	168.428	0.630
S71	-5.393	0.049	-9.191	0.049	-149.594	0.264
S175	1.688	0.079	-5.430	0.079	162.729	0.7912

Note. Following the stellar designation in column (1), we list consecutively the following quantities with their uncertainties: slopes of the R.A. and decl. data as a function of time and the corresponding position angles ϕ .

(This table is available in machine-readable form.)

Table 5
Position Angles of the Red Disk

Star	$m1(t, \text{R.A.})$ (mas yr ⁻¹)	$\Delta m1$ (mas yr ⁻¹)	$m2(t, \text{decl.})$ (mas yr ⁻¹)	$\Delta m2$ (mas yr ⁻¹)	Φ (deg)	$\Delta\Phi$ (deg)
1.	2.	3.	4.	5.	6.	7.
S4	-22.725	0.305	-4.321	0.305	-100.766	0.755
S6	-14.624	0.161	-1.734	0.161	-96.761	0.628
S14	-17.048	0.510	-15.601	0.510	-132.461	1.265
S18	18.905	0.443	13.206	0.443	55.064	1.101
S21	26.326	0.557	5.246	0.557	78.730	1.189
S22	-5.898	0.024	1.998	0.024	-71.287	0.219
S23	22.507	0.392	2.768	0.392	82.990	0.990
S33	15.026	0.100	-1.445	0.100	95.493	0.378
S38	29.086	0.919	1.432	0.919	87.182	1.809
S54	11.014	0.048	5.224	0.048	64.624	0.228
S66	-9.965	0.028	-0.174	0.028	-91.001	0.161
S67	10.856	0.044	0.054	0.044	89.715	0.232
S83	9.884	0.029	2.013	0.029	78.486	0.166
S85	4.688	0.005	-1.380	0.005	106.407	0.058
S87	-5.897	0.010	2.186	0.010	-69.664	0.094
S89	11.564	0.067	8.097	0.067	55.001	0.274
S91	-7.563	0.017	0.848	0.027	-83.604	0.128
S96	8.376	0.026	-2.054	0.026	103.781	0.174
S97	-7.486	0.013	1.026	0.013	-82.195	0.101
S145	11.179	0.046	1.170	0.046	84.023	0.235

Note. Following the stellar designation in column (1), we list consecutively the following quantities with their uncertainties: slopes of the R.A. and decl. data as a function of time and the corresponding position angles ϕ .

(This table is available in machine-readable form.)

Table 6
Position Angles of the Linear Stellar Trajectories

Star	$m1(t, \text{R.A.})$ (mas yr ⁻¹)	$\Delta m1$ (mas yr ⁻¹)	$m2(t, \text{decl.})$ (mas yr ⁻¹)	$\Delta m2$ (mas yr ⁻¹)	Φ (deg)	$\Delta\Phi$ (deg)
1.	2.	3.	4.	5.	6.	7.
S5	-6.121	0.207	7.610	0.318	-38.813	1.502
S7	-3.768	0.063	-1.826	0.117	-115.849	1.494
S10	-4.823	0.090	3.667	0.059	-52.752	0.677
S11	8.486	0.152	-4.849	0.241	119.743	1.303
S20	-4.661	0.203	-5.363	0.214	-139.005	1.675
S25	-2.441	0.105	1.724	0.181	-54.768	3.063
S26	5.700	0.131	1.930	0.157	71.292	1.475
S27	0.215	0.143	3.609	0.173	3.416	2.261
S28	4.381	0.412	5.065	0.392	40.860	3.452
S30	0.318	0.102	3.296	0.098	5.504	1.757
S32	-3.609	0.125	-0.199	0.238	-93.150	3.774
S34	9.899	0.209	4.441	0.156	65.837	0.876
S35	1.834	0.097	3.727	0.187	26.197	1.656
S36	0.268	0.246	-1.360	0.431	168.848	10.561
S37	-6.324	0.351	9.605	0.283	-33.359	1.653
S40	4.172	0.585	5.165	0.935	38.929	6.414
S41	1.331	0.130	-3.197	0.182	157.405	2.302
S43	5.119	0.177	6.135	0.430	39.839	2.201
S44	-6.662	0.559	-8.450	0.589	-141.746	3.038
S45	-5.688	0.162	-4.037	0.117	-125.363	1.100
S46	0.966	0.186	4.566	0.161	11.950	2.268
S47	-3.058	0.448	2.789	0.186	-47.633	4.594
S48	-1.626	0.212	10.040	0.418	-9.198	1.238
S49	15.222	0.268	-0.760	0.664	92.859	2.494
S50	-1.370	0.362	10.459	0.327	-7.462	1.963
S51	8.422	0.509	7.655	0.397	47.730	2.273
S52	4.627	0.501	-5.721	0.298	141.033	3.369
S53	7.096	0.366	9.465	0.504	36.860	2.039
S56	-18.748	0.685	-1.319	0.411	-94.026	1.259
S57	-9.770	0.521	-0.312	0.360	-91.828	2.112
S58	7.686	0.356	5.449	0.202	54.667	1.603
S59	7.458	0.375	-1.606	0.342	102.154	2.579
S61	-4.487	0.561	-6.718	1.017	-146.258	5.195
S63	-13.15	0.847	4.335	0.549	-71.755	2.419
S65	2.401	0.097	-1.616	0.124	123.940	2.305
S68	3.971	0.236	3.108	0.148	51.946	2.119
S69	-1.786	0.207	2.052	0.558	-41.037	8.384
S70	-4.141	0.235	-3.600	0.263	-131.006	2.626
S72	9.101	0.200	-5.645	0.133	121.811	0.825
S73	-9.223	0.245	-7.771	0.156	-130.115	0.941
S74	-0.170	0.209	5.026	0.242	-1.941	2.380
S75	7.138	0.249	2.330	0.321	71.921	2.404
S76	-3.329	0.182	4.898	0.161	-34.201	1.700
S77	9.536	0.439	-6.606	0.524	124.711	2.460
S78	-16.728	0.429	-5.989	0.360	-109.697	1.190
S79	0.040	0.218	4.269	0.449	0.536	2.932
S80	-4.640	0.221	6.325	0.435	-36.261	2.288
S81	5.072	1.908	6.529	0.739	37.842	10.906
S82	-8.689	0.329	-14.942	0.373	-149.821	1.128
S84	3.926	0.084	1.282	0.218	71.916	2.903
S86	-0.892	0.308	-4.872	0.392	-169.627	3.601
S88	-3.941	0.265	-7.715	0.227	-152.939	1.702
S90	1.713	0.349	1.266	0.228	53.536	7.452
S92	5.530	0.095	2.238	0.303	67.966	2.718
S93	-2.972	0.349	-1.755	0.374	-120.553	6.099
S94	-13.564	0.513	2.089	0.735	-81.243	3.052
S95	5.273	0.295	0.987	0.101	79.402	1.208
S98	-7.985	0.186	1.922	0.284	-76.465	1.947
S99	-10.093	0.459	0.240	0.336	-88.638	1.906
S100	-1.392	0.202	-2.557	0.200	-151.432	3.969
S101	2.168	0.422	5.836	0.400	20.376	3.864
S102	-5.376	0.594	8.018	0.512	-33.842	3.380

Table 6
(Continued)

Star	$m1(t, \text{R.A.})$ (mas yr ⁻¹)	$\Delta m1$ (mas yr ⁻¹)	$m2(t, \text{decl.})$ (mas yr ⁻¹)	$\Delta m2$ (mas yr ⁻¹)	Φ (deg)	$\Delta\Phi$ (deg)
1.	2.	3.	4.	5.	6.	7.
S103	11.849	0.405	-3.727	0.736	107.463	3.288
S104	10.255	0.344	-2.270	0.507	102.481	2.733
S105	3.908	0.336	-7.620	0.482	152.849	2.484
S106	1.135	0.275	-0.981	0.570	130.845	17.841
S107	-0.580	0.112	4.581	0.228	-7.217	1.426
S108	3.868	0.420	0.449	0.422	83.377	6.208
S109	7.021	0.374	-4.926	0.278	125.050	2.089
S110	-2.956	0.267	-1.221	0.251	-112.442	4.534
S111	-2.490	0.245	-7.337	0.255	-161.253	1.819
S112	3.062	0.439	10.822	0.341	15.797	2.205
S146	-3.465	0.905	-0.189	0.986	-93.118	16.281

Note. Following the stellar designation in column (1), we list consecutively the following quantities with their uncertainties: slopes of the R.A. and decl. data as a function of time and the corresponding position angles ϕ .

(This table is available in machine-readable form.)

motion speed and direction. Their inclusion in the presented discussion awaits the determination of orbital elements. For completeness, we list the kinematic properties of these stars in the appended table (appended Table 6).

3. Discussion

A close inspection of the orbital parameters showed that the stars in the central arcseconds are arranged in two orthogonal disks. There are three observational facts that support this finding:

1. The distribution of inclinations clustering around 90° . This shows that stellar orbits are seen preferentially edge on.
2. The distribution of semimajor axes of the projected ellipses in the sky shows that the stars populating the disks can indeed be separated into two groups.
3. The observation of accumulation of orbits that appear face on or edge on from certain directions shows the presence of two orthogonal stellar disks.

In the following, we describe these findings in more detail and then highlight present stellar dynamical concepts that may explain the phenomenon.

3.1. Histograms and Visualizations

3.1.1. Orbital Inclinations

In Figure 2, we show that the inclinations derived by us and those provided by Gillessen et al. (2017) are in very good agreement. The same can be said for all of the other orbital elements shown in Figure 2. In Figure 3, we show the distribution of all 39 stars with orbital fits in comparison to a $\sin i$ distribution as one might have expected for a fully uniformly randomized scenario. Here, $\sin i$ refers to the expected shape of the uniformly distributed inclination angles and not the trigonometric sine function of the angle. This ideal shape is also referred to as the Gilbert-sine distribution (Gilbert 1895). In Figure 3, both distributions are normalized to an integral value of unity. Compared to the $\sin i$ distribution, the measured distribution shows a deficit of stars with inclinations in the intervals 0° – 20° and 160° – 180° . It also

has a full width at half-power of around only 80° , although one would expect a width of about 100° for a $\sin i$ distribution. In addition, the measured distribution shows an excess of stars around inclinations of 80° – 140° . The preference for high inclinations can also not be due to a field-of-view effect due to the small size of the S cluster within the large GC stellar cluster (see Appendix A). Also, biases for the orbital elements due to incomplete orbital coverage are not important for the analysis of our problem (see Appendix B). Hence, this comparison shows that in the set of 39 S-cluster stars, edge-on orbits are preferred.

3.1.2. Distribution of Orbits in Space

In Figure 4, we show the three-dimensional distribution of the orbits. In all projections, the two organization of two orthogonal disks (black and red) of the stars is apparent. The coloring is based on visual inspection of perpendicularity in three dimensions. In Figures 4(a)–(d), we show the orbits using the complete set of orbital elements. In Figures 4(e)–(h), we show the circularized orbits after the eccentricity had been set to zero and the long orbital axes had been set to a constant value. In this version, only the orbital angles are preserved and the bunching into orbital families becomes most apparent. In Figures 4(a) and (e), the face-on view as seen from Earth is presented. In this case, the black orbital family is seen almost edge on. In Figures 4(b) and (f), the set of orbits has been rotated by 25° from elevations -90° to -115° . Here, the two orbital families are both seen edge on. In Figure 5, we show a smoothed version of the pole vision for the circularized orbits in Figure 4(f). Here, the X-shape structure of the two disks can be seen more clearly. In Figures 4(c) and (g), the set of orbits has been rotated by -100° in azimuth (keeping the elevation at 0). In this case, the black orbital family is seen face on while the red orbital family is edge on. In Figures 4(d) and (h), we rotated to elevation -25° (and azimuth at 0°) such that the red system is then seen face on and the black system is edge on.

The two orbital disk systems are well separable (see above) but rather thick. Furthermore, the orthogonal X-shaped disk structure becomes apparent only in alternating zones in the position angle histogram (see Figure 8) and in Ω diagrams as well (see Figure 6). This leads to the fact that they cannot easily

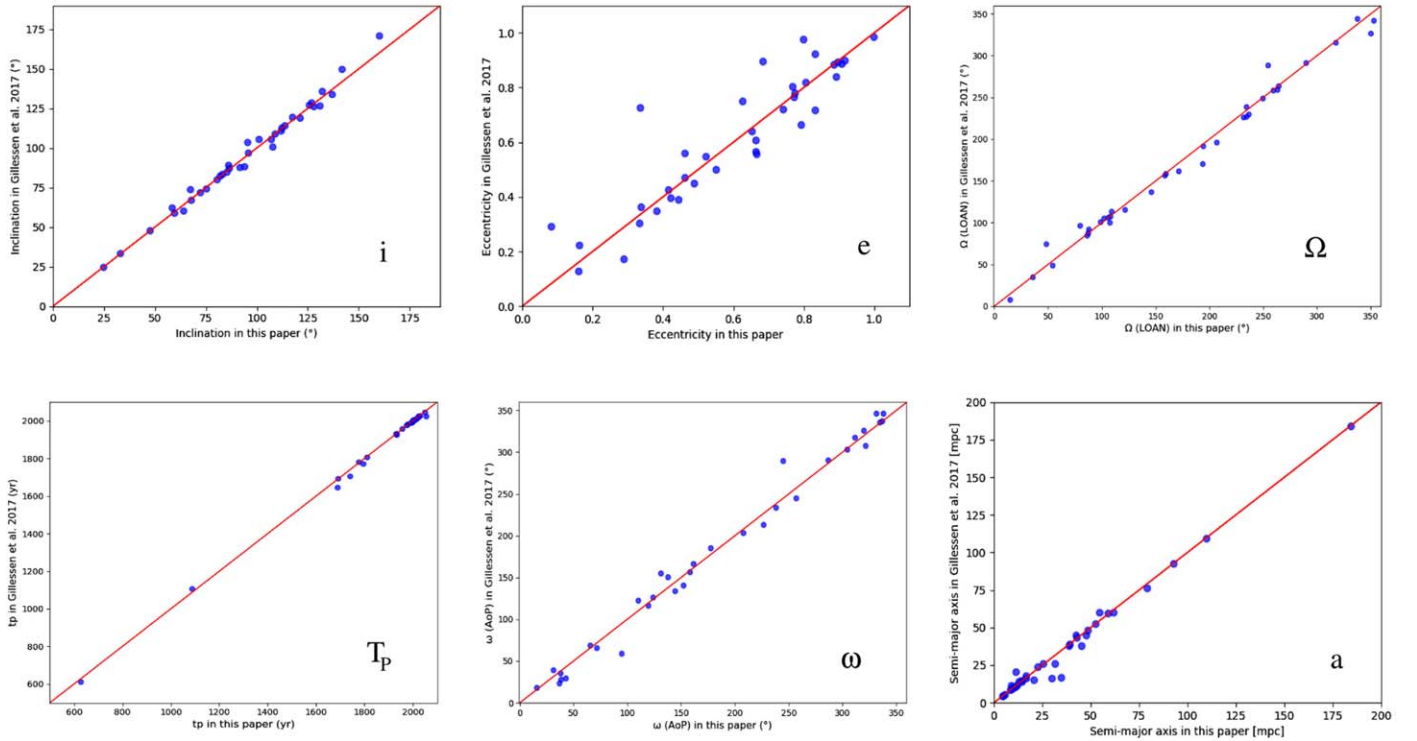


Figure 2. A comparison between the orbital elements listed by Gillessen et al. (2017) and in this paper.

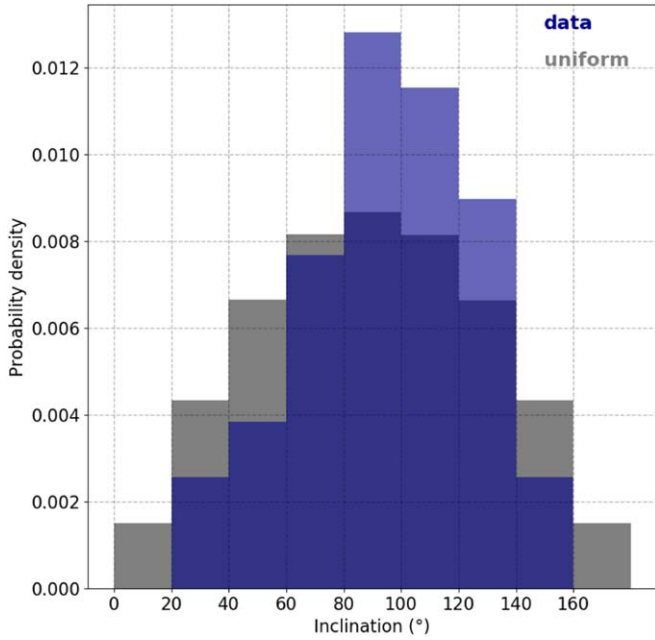


Figure 3. A comparison between the measured distribution of orbital inclinations and the expected $\sin i$ distribution.

be recognized in polar diagrams as used by, e.g., Gillessen et al. (2017) in their Figure 12 or Yelda et al. (2014) in their Figure 21. In Figure 6, we show the inclination of the stars as a function of the longitude of the ascending node Ω . The color indicates their membership in either the red or the black disk. It becomes clear that the two disks cannot easily be identified as the angular momentum vectors of the disk members point in opposite directions. Comparing Figure 8 and Figure 6, one can

also see that the two disks can be better separated by evaluation in the position angle histogram instead of evaluating the longitude of the ascending node Ω .

However, compared to Figure 6, the inclined and face-on representations of the disk members as shown in Figure 4 are better grouped together, because the direction of the angular momentum vector is not relevant in this representation.

Here, looking at circularized orbits as described above is more successful in searching for face-on orbits that bunch close to the circumference of the sky-projected distributions as in Figures 4(g) or (h).

In Figures 7(a) and (b), we show the inclinations of the two stellar systems. On the right-hand side of Figure 7, we show the distribution of inclinations for all stars within the central arcseconds for which we can provide Newtonian orbital fits. In particular, the distributions for the two disks do not follow a $\sin i$ distribution as one might have expected for a fully randomized scenario. There is a clear clustering of inclinations around a mean value of $\sim 90^\circ$ with the bulk of the higher inclined stellar orbits contained within an interval width of 50° (red disk with bulk between 80° and 130°) or even a width of only 40° (black disk with bulk between 70° and 110°). In comparison to the expected width of about 100° for a $\sin i$ distribution, this implies that the two separate disk are highly biased toward high inclinations. There are also no stars with inclinations in the intervals 0° – 20° and 160° – 180° .

It follows that the S-cluster stars for which we obtained orbits are organized in two highly inclined disk systems that are arranged in an X shape.

3.1.3. Distribution of Orbits in the Sky

As most stars have high inclinations, the relative orientation of their orbits in the sky can be investigated by comparing the

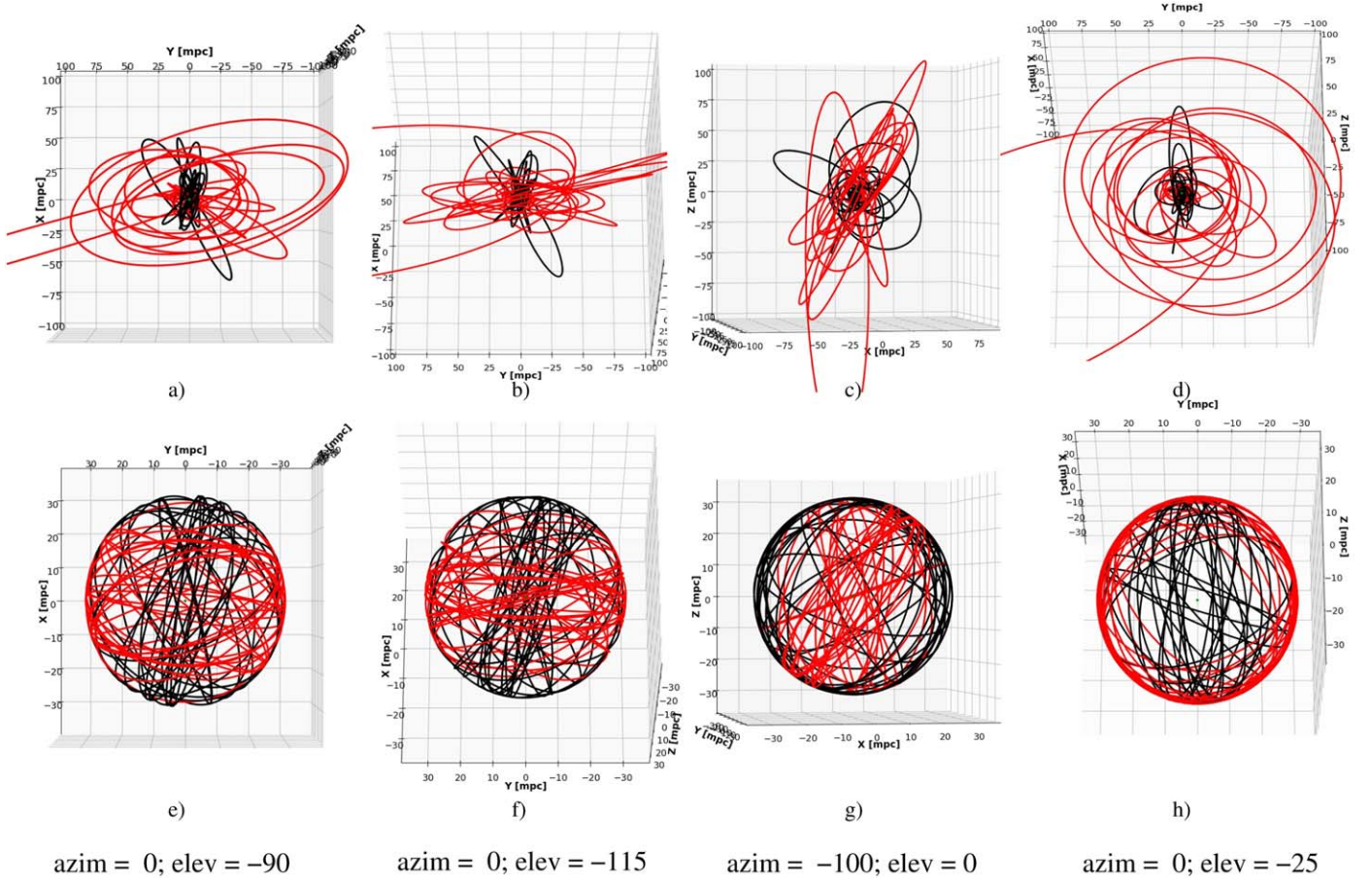


Figure 4. Visualizations of the distribution of all 39 orbits of the S-cluster stars. In the top row, the orbital elements as derived from the observational data are used. In the bottom row, the ellipticities have been set to zero and the semimajor axes have been set to a constant value. Hence, only the orientation angles of the orbits are relevant for the visualization. The azimuthal and elevation angles for the corresponding projections are given. Panels (b) and (f) show both disk systems seen edge on. In (c) and (g), the orbits of the black system are face on, and those of the red system are edge on. Finally, panels (d) and (h) show the red system face on, the black system edge on. We refer also to the animation that shows the projected orbital arrangements in motion in Figure 17.

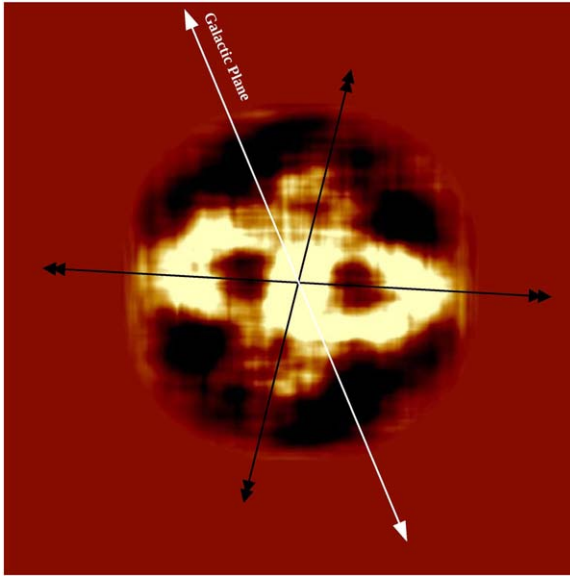


Figure 5. Smoothed representation of the pole vision image of the circularized orbit distribution shown in Figure 4(f). We subtracted the distribution expected from 39 randomly oriented orbits. Here the 39 orbits are generated, assuming a $\sin i$ uniform distribution for the inclinations, and a circular uniform distribution of the longitude of ascending node after setting $e = 0$ and $a = \text{const}$. As in Figure 4(f), the black lines indicate the directions of the disks and the white line the direction of the Galactic plane.

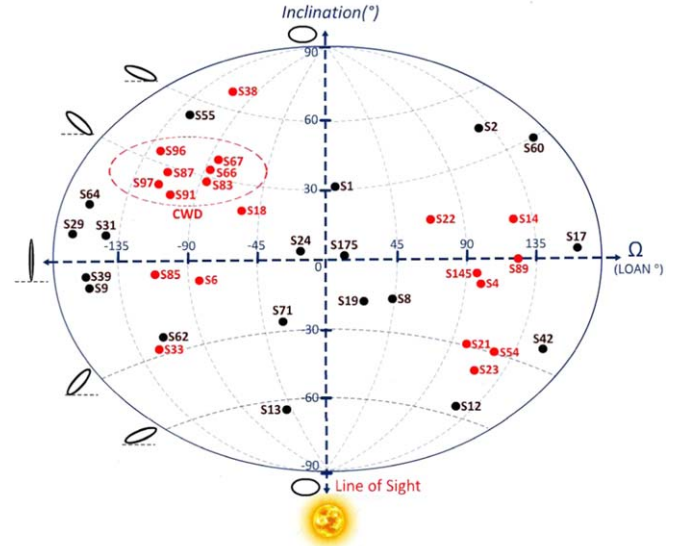


Figure 6. The inclination as a function of the (LOAN) longitude of the ascending node Ω .

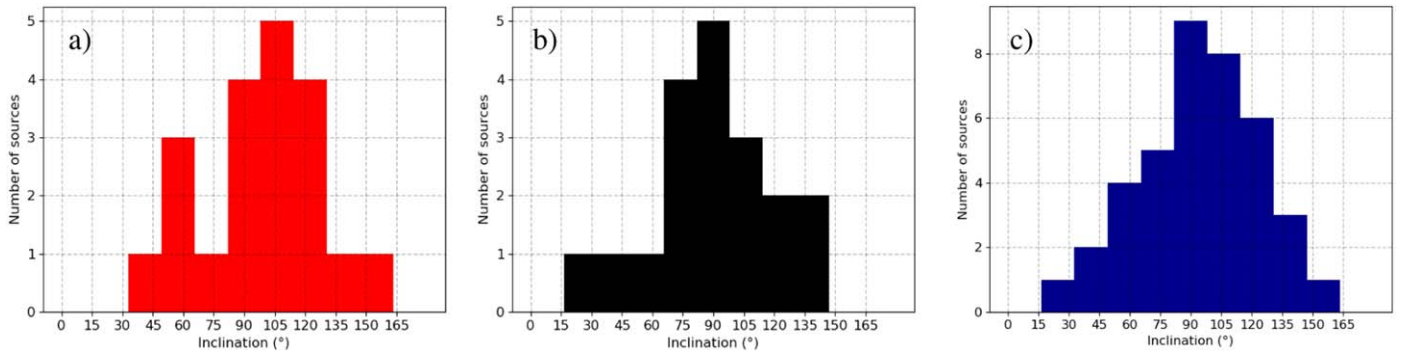


Figure 7. Inclination angles of all 39 stars with known orbits. We find that most of the orbits are highly inclined and seen almost edge on. (a) Red disk: inclination angles of all 20 stars, which orbit in the east–west disk. (b) Black disk: inclination angles of all 19 stars, which orbit in the north–south disk. (c) All stars in a combined histogram.

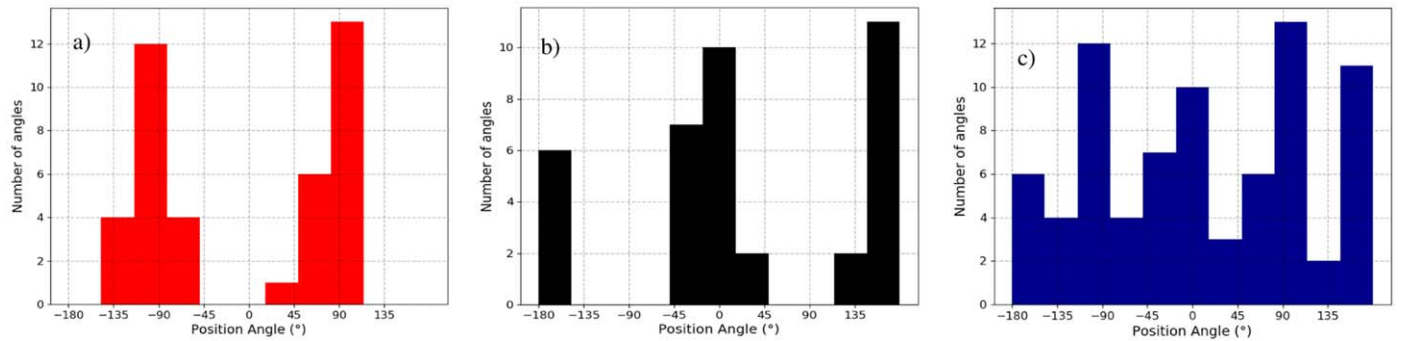


Figure 8. The distributions of the position angles of the semimajor axes of the sky-projected orbits show that the orbits of the stars in the red and black systems are orthogonal to each other. (a) Position angles of the 19 stars, which orbit in the black north–south disk. (b) Position angles of the 20 stars, which orbit in the red east–west disk. (c) Position angles of all 39 stars with known orbits.

position angles of the semimajor axes of their sky-projected orbits.

In Figure 9(a), we show the position angles of the sky-projected orbital ellipses in a circular histogram. The orthogonal red and black orbital families are apparent. In Figure 9(b), we show the same diagram consisting of lines indicating the same position angles but now smoothed with a circular Gaussian with a width corresponding to about one-fifth of the line length. Here, the representation of the line density is enhanced. Both stellar disks have an angle of about 45° with respect to the Galactic plane.

The stars can clearly be separated into two groups (black and red) that form two stellar disks oriented almost perpendicular to each other. In Figure 8, we show how the position angles of the projected orbits are distributed for the two disks and for all of the 39 stars. Each of the position angles is supplemented by a second angle separated by 180° . Through this we account for the fact that the stars will ascend and descend on their highly elliptical orbits. The total number of angles considered in Figure 8 is 78.

The red disk clusters around $\pm 90^\circ$, while the black disk is concentrated around the angles 0° and $\pm 180^\circ$. In order to investigate the statistical significance of this arrangement, we need to apply methods that have been developed for directional statistical analysis. Starting with the multimodal distribution of position angles, we can apply Rao’s spacing test (Jammalamadaka & SenGupta 2001). The test is based on the

idea that if the underlying distribution is uniform, then the observation of N successive directions should be approximately evenly spaced. They should show an angular separation of about $360^\circ/N$. Large deviations from this distribution, resulting from unusually large spaces or unusually short spaces between the observed directions, are evidence for directionality. The test is more powerful than the Rayleigh test (Durand & Arthur 1958) when it comes to multimodal distributions. After placing all 78 position angles on a circle, we performed the test and the resulting p -value is 0.01 with a test statistic of 154.12 and a critical statistic of 152.46, allowing us to reject the hypothesis that the distribution is uniform. In addition, we performed the Hodges–Ajne test (Ajne 1968; Bhattacharayya & Johnson 1969) for uniformity of a circular distribution. The test is based on the idea that if the number of points in an arc exceeds the expected number for a uniform distribution, then the hypothesis is rejected. The implemented Hodges–Ajne test in Python returns either 1 or 0 as a p -value. Applying it to our position angle distribution, we obtained a p -value of 0.

Hence, they can be separated very well. Thanks to the high inclination of the orbits, the pole of this distribution (i.e., the region where most orbits cross each other) is close to the line of sight and the two stellar systems can be separated even in their direct projected appearance in the sky. The same can be done with the projection of the semimajor axes of the three-dimensional orbits, as shown in Figure 9(c). To get a clear view, we rotate the orbital arrangement close to the pole vision

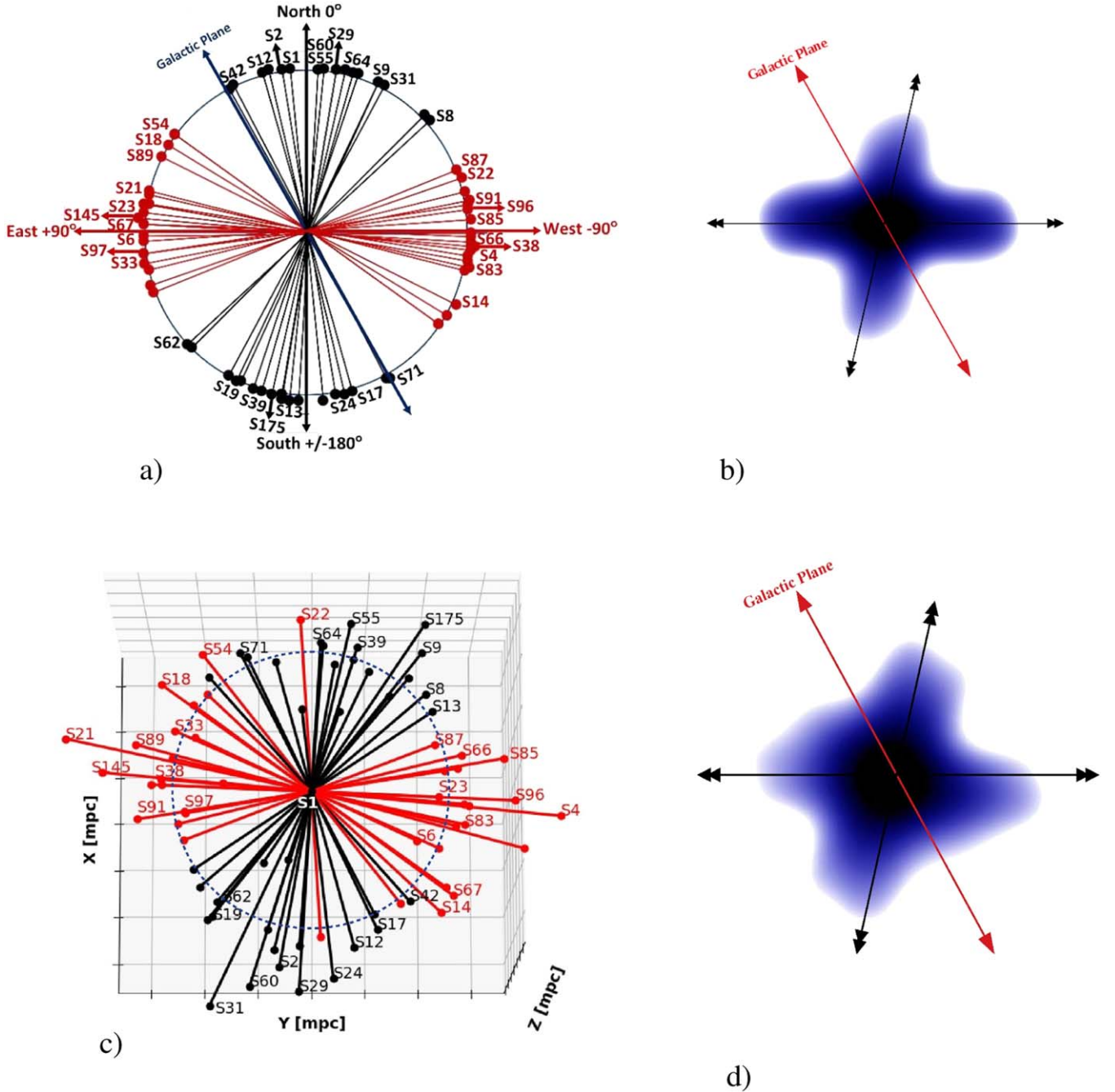


Figure 9. Angular arrangement of the disks for all 39 stars for which we have orbital solutions. We labeled the lines for all stars. (a) Here we show for all stars the position angles of the semimajor axes of their sky-projected orbits. The shape of the two disks is remarkably clear. (c) The position angles of the projected semimajor axes of the three-dimensional orbits of all stars after rotation close to the pole vision of the system. The X shape is observed in the range between elevation -90° and -115° but most clearly close to elevation -100° . The two disks are well separable. (b) and (d) are the same as in (a) and (c), but smoothed with a circular Gaussian of a width corresponding to about one-fifth of the line length in figure section (a) and (c). For (d), only the position angle line in (c) inside the dashed circle has been used for the convolution.

and use the projected semimajor axes of the orbits. The smoothed version of the distribution is shown in Figure 9(d).

We note that the trend of having two orthogonal disks is probably also continued toward stars with separations to Sgr A* smaller than those of the star S2. The recently found high-velocity star S62 (Peißker et al. 2020) lies to within 30° close to the black disk. This star has separation from Sgr A* ranging between 17.8–740 au, compared to S2 with 120–970 au. We expect to find stars close to the red disk with similarly short periods and small distances to Sgr A*.

This shows that the highly inclined stellar orbits can indeed be separated into two groups that represent two orthogonal disks.

3.1.4. Orbital Eccentricities

Gillessen et al. (2017) find that the distribution of eccentricities of the S-star cluster is thermal, which is in agreement with Figure 10(c). However, this obviously does not necessarily imply that the orbits are randomly oriented. The two disk systems show that the S-star cluster is highly

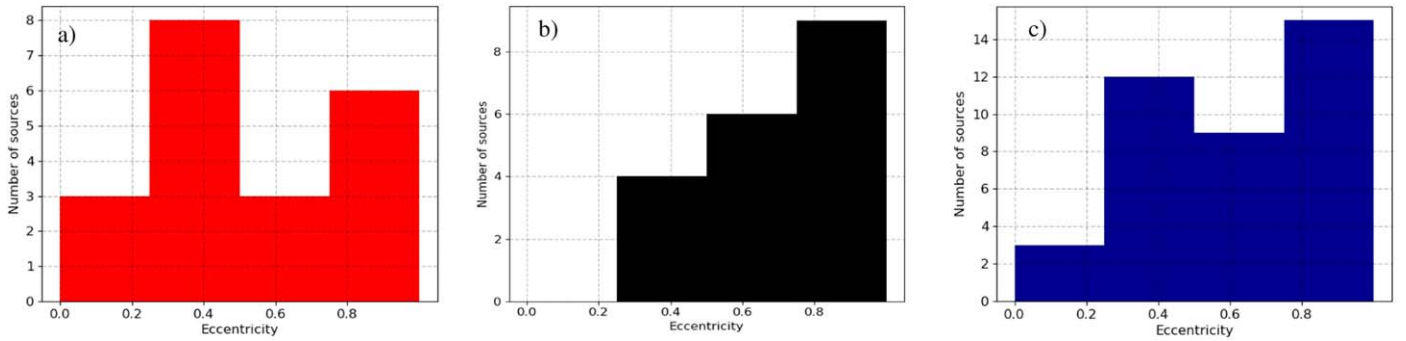


Figure 10. (a) Eccentricities of the 20 stars, which orbit in the red east–west disk. (b) Eccentricities of the 19 stars, which orbit in the black north–south disk. (c) Eccentricities of all 39 stars with known orbits (including the seven exmembers).

organized. In Figures 10(a) and (b), we show the histogram of eccentricities for the two disk systems. There are only about half the number of sources in the individual histograms; however, within the uncertainties, we find at least for the black disk a distribution that is consistent with a thermal distribution. The distribution of the red disk is much flatter and is even biased toward the low-ellipticity side of the diagram, i.e., toward the less thermal side. This would imply a more thermal, relaxed distribution as expected from the Hills mechanism (Hills 1988) for the black disk. For the red disk, the implication is that it is more influenced by a disk-migration scenario as it approaches the less-than-thermal side of the graph. This is consistent with the fact that the black disk is more compact—it is confined to within a radius of about $1''$ —and the red disk is significantly larger, with stars confined to within a $2.''3$ radius. However, while at first glance it may be coupled to the CWD of He stars (Levin & Beloborodov 2003; Paumard et al. 2006), it is likely to have a different origin or history because the angular momentum vectors for individual stars in each disk point in opposite directions. Here, the scattering of resonance mechanisms may be more important than at larger distances from Sgr A* (see discussion in Section 3.2.1).

It is not clear if and how the more compact black disk is coupled to the counterclockwise disk claimed to be perpendicular to the CWD (Paumard et al. 2006). How the two stellar disks are arranged in projection against the sky and the GC stellar cluster is shown in Figure 11.

3.2. Stellar Dynamical Considerations

Stars bound to an SMBH interact gravitationally. The reason for the nonisotropic distribution of S-cluster members may be inferred by comparing the characteristic timescales of different dynamical processes (nonresonant two-body relaxation, resonant relaxation) with the estimated age of S stars. For the S2 star, Habibi et al. (2017) derive an age of $6.6^{+3.4}_{-4.7}$ based on 12 years of spectroscopic monitoring, with the cumulative signal-to-noise ratio of $S/N > 200$, with an upper limit on the formation time of S stars of < 15 Myr. This is consistent within uncertainties with the formation time of the clockwise (CW) disk of young, massive OB/WR stars, 5 ± 1 Myr, which occupies the region beyond the S cluster at the deprojected distance between ~ 0.04 and 0.5 pc (Genzel et al. 2010). This suggests a common origin of massive OB stars in the CW disk and those of lighter S stars of spectral-type B.

Recently, a group of NIR-excess compact sources was identified (Eckart et al. 2013), whose spectral properties, in particular for the intensively monitored DSO/G2 object (Gillessen et al. 2012; Witzel et al. 2014; Valencia-S. et al. 2015), suggest that these could be pre-main-sequence stars of Class I source with an even younger age of ~ 0.1 – 1 Myr (Zajaček et al. 2017). If DSO/G2, G1 object and other NIR-excess sources are pre-main-sequence stars of class I (with the age of ~ 0.1 – 1 Myr), then their orbits should also keep dynamical imprints of the initial formation process, e.g., most likely an infall of the molecular clump and a subsequent in situ star formation (Jalali et al. 2014). In that case, NIR-excess sources could form a dynamically related group of objects, e.g., their inclinations would be comparable, which can be tested observationally in the future when orbital elements for more objects will be inferred. In case additional gas infall occurred after the stellar disk formation, its effect is “superimposed” on the dynamical effect any residual disk gas could have had. The evidence for the inspiral of fresh gas is supported by Yusef-Zadeh et al. (2013, 2017), who identified traces (SiO outflows, bipolar outflows) of recent star formation (10^4 – 10^5 yr ago) in the inner parsec. In addition, the discovery of the population of compact NIR-excess sources (DSO, G1 etc.) supports the theory of recent and ongoing star formation and molecular gas replenishment in the inner parsec.

3.2.1. Basic Dynamical Timescales

The population of S stars consisting of two disks is not relaxed, hence any current configuration is subject to resonant and nonresonant relaxation processes in the nuclear star cluster. The configuration of two perpendicular stellar disks can be stable over a timescale of 10^8 yr as demonstrated in the simulations by Mastrobuono-Battisti et al. (2019) that we refer to later. In the current section, we mention key dynamical processes that might have contributed to the X structure and so far could have influenced it. In particular, the resonant relaxation process can lead to the spread in orbital inclinations in each disk. An important quantity to understand the dynamics of a stellar system is the relaxation timescale within which a system reaches a statistical equilibrium through stellar interactions. Persistent torques acting between the orbits of the S stars will lead to the rapid resonant relaxation of the orbital orientation vectors (vector resonant relaxation) and the slower relaxation of the eccentricities (scalar resonant relaxation). These mechanisms both act at rates much faster than two-body

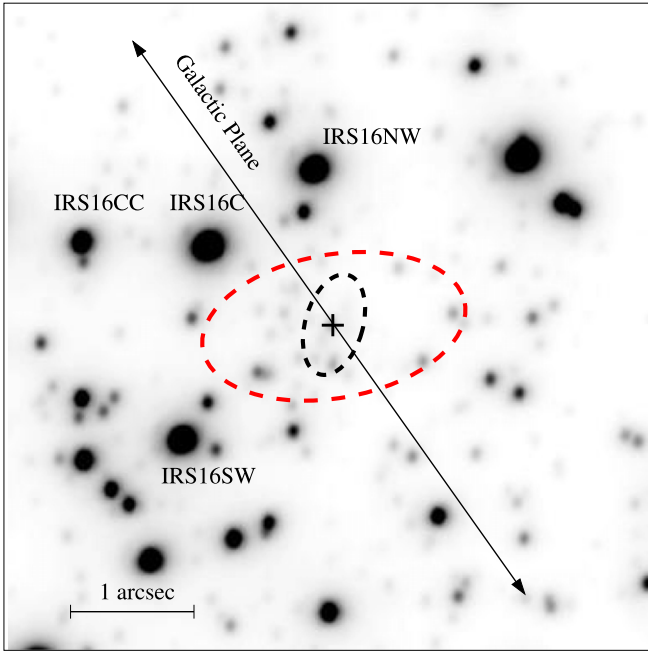


Figure 11. Location and extent of the red and black stellar disks with respect to the GC stellar cluster and the Galactic plane. Sgr A* is located at the center of the open cross close to S2. East is to the left, north is up. The semimajor axis of the black (red) dashed ellipse is about twice the median of $0''.4$ or 16 mpc ($1''.18$ or 47 mpc), the semimajor axes of all orbits attributed to the black (red) disk system. The minor axes of the ellipses have been chosen such that they include the central half of the corresponding disk system orbits. The red dashed line comprises the bulk of the S-cluster stars. The epoch of the underlying image is early 2018.

or nonresonant relaxation. Possible physical sources of orbit perturbations are discussed in Section 3.2.2.

(a) *Resonant relaxation timescales*

To calculate typical timescales, we adopt the relations presented by Hopman & Alexander (2006). The nonresonant relaxation timescale dominated by two-body interactions can be expressed as follows:

$$T_{\text{NR}} = A_{\Lambda} \left(\frac{M_{\bullet}}{M_{\star}} \right)^2 \frac{P(a)}{N(<a)}, \quad (1)$$

where $P(a) = 2\pi [a^3/(GM_{\bullet})]^{1/2}$ is the Keplerian orbital period and A_{Λ} is a dimensionless factor that contains the Coulomb logarithm. $N(<a)$ is the number of stars with semimajor axes smaller than a given semimajor axis a . For stellar mass M_{\star} , we take $M_{\star} = 10 M_{\odot}$, which is the order of magnitude estimated for several S stars (Genzel et al. 2010; Habibi et al. 2017).

For *scalar resonant relaxation*, which changes the value of the angular momentum $|J|$, we consider the typical timescale in the following form:

$$T_{\text{RR},s} = \frac{A_{\text{RR},s}}{N(<a)} \left(\frac{M_{\bullet}}{M_{\star}} \right)^2 P^2(a) |1/t_{\text{M}} - 1/t_{\text{GR}}|, \quad (2)$$

where the factor $A_{\text{RR},s} = 3.56$ is inferred from N -body simulations of Rauch & Tremaine (1996). The timescales t_{M} and t_{GR} correspond to the mass precession and to the general

relativity (GR) timescale, respectively. The mass precession takes place due to the potential of an extended stellar cluster and may be expressed as

$$t_{\text{M}} = A_{\text{M}} \frac{M_{\bullet}}{N(<a)M_{\star}} P(a), \quad (3)$$

where the factor A_{M} is of the order of unity. Closer to the black hole associated with Sgr A*, the GR precession is the dominant effect, which takes place on the timescale of t_{GR} ,

$$t_{\text{GR}} = \frac{8}{3} \left(\frac{J}{J_{\text{LSO}}} \right)^2 P(a), \quad (4)$$

where $J_{\text{LSO}} \equiv 4GM_{\bullet}/c$ is the angular momentum of the last stable orbit.

Vector resonant relaxation keeps the magnitude but changes the direction of the angular momentum J . The timescale of the vector resonant relaxation can be estimated as

$$T_{\text{RR},v} \simeq 2A_{\text{RR},v} \left(\frac{M_{\bullet}}{M_{\star}} \right) \frac{P(a)}{N^{1/2}(<a)}, \quad (5)$$

where the factor $A_{\text{RR},v} = 0.31$ (Rauch & Tremaine 1996).

Another process that induces the eccentricity–inclination oscillations is the Kozai–Lidov mechanism, which involves three bodies, i.e., the inner binary system (black hole–star) perturbed by a stellar or a gaseous disk (Šubr & Karas 2005) or an inner binary (star–star) perturbed by the black hole (Stephan et al. 2016). The timescale of Kozai–Lidov oscillations induced by a self-gravitating disk having the mass of M_r at the distance of r from the Galactic center is (Šubr & Karas 2005; Hopman & Alexander 2006)

$$T_{\text{KL}} = 2\pi \left(\frac{M_{\bullet}}{M_r} \right) \left(\frac{r}{a} \right)^3 P(a). \quad (6)$$

For quantitative estimates, we used a specific mass density profile of stars $\rho_{\star}(r)$ to calculate timescales expressed by Equations (1)–(6). We adopted a broken power-law profile according to (Schödel et al. 2009; Antonini et al. 2012)

$$\rho_{\star} = \rho_0 \left(\frac{r}{r_b} \right)^{-\gamma_s} \left[1 + \left(\frac{r}{r_b} \right)^2 \right]^{(\gamma_s - 1.8)/2}, \quad (7)$$

where γ_s is the inner slope, and r_b is the break radius, for which we take $r_b = 0.5$ pc. Setting $\rho_0 = 5.2 \times 10^5 M_{\odot} \text{ pc}^{-3}$ gives the integrated, extended mass in accordance with Schödel et al. (2009), within their inferred range of $\sim (0.5\text{--}1.5) \times 10^6 M_{\odot}$ (with the black hole mass subtracted). We consider two cases for the inner slope:

1. $\gamma_s = 1.0$, which is consistent with the volume density of the S cluster, $\rho_s \propto r^{-1.1 \pm 0.3}$, based on the orbits of 15 stars with the semimajor axis of $a \lesssim 0''.5$ (Genzel et al. 2010),
2. $\gamma_s = 0.5$, which represents the overall observed stellar distribution in the central parsec (Buchholz et al. 2009).

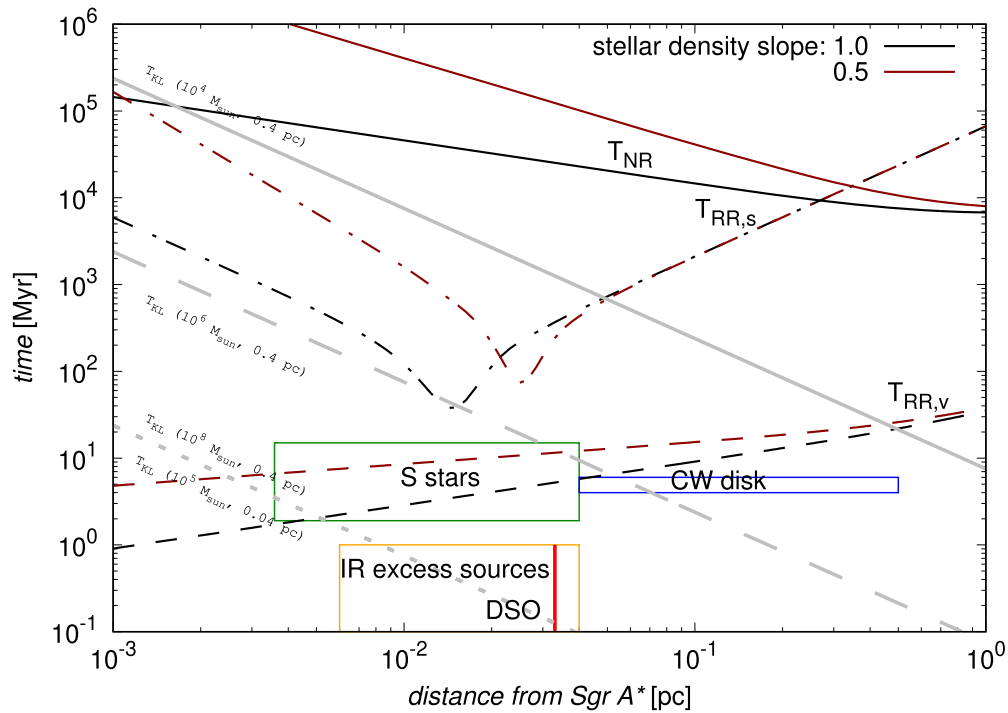


Figure 12. The time in millions of years (Myr) vs. the semimajor axis in parsecs (pc) for the inner slope of the stellar-density distribution equal to $\gamma_s = 0.5$ and $\gamma_s = 1.0$, which are depicted by different colors, dark red and black, respectively. Different lines correspond to the estimates of typical timescales of dynamical processes operating in the central parsec: T_{NR} corresponds to nonresonant relaxation (solid black and dark-red lines), $T_{RR,s}$ stands for scalar resonant relaxation (dotted-dashed black and dark-red lines), $T_{RR,v}$ for vector resonant relaxation (dashed black and dark-red lines), and T_{KL} for Kozai–Lidov timescales (gray solid, long-dashed, and short-dashed lines, depending on the mass and the distance of the stellar disk). All timescales are calculated according to relations given in Equations (1)–(6) for the individual stellar mass of $M_* = 10 M_\odot$ when relevant. The distinct minimum time for scalar resonant relaxation corresponds to the semimajor axis, where GR precession takes over the extended Newtonian-mass precession. The values in parentheses next to the Kozai timescale, e.g., $T_{KL}(10^4 M_\odot, 0.4 \text{ pc})$, represent the parameters of the massive gaseous or stellar disk, in particular $M_t = 10^4 M_\odot$, which is at the distance of $r = 0.4 \text{ pc}$; see also Equation (6). The rectangles stand for the distance as well as the determined age of different stellar populations, namely S stars, CW-disk stars, and NIR-excess sources; specifically, the DSO is represented by the thick solid red line. The inner radius of the S-cluster box is now represented by the S62 semimajor axis (Peißker et al. 2020).

Using the two stellar distributions, we show the timescale estimates alongside the characteristic stellar structures (S stars, CW disk, DSO, and other NIR-excess sources) in the time–semimajor axis plot, see Figure 12.

We adopt the age constraints of S stars from the recent spectroscopic study of Habibi et al. (2017), where they show that S stars are young and comparable in terms of age to OB stars from the CW disk. However, it is premature to claim that these two populations are identical in terms of age. They could have formed in two separate star formation events, with a different dynamical configuration.

The findings in this work, in particular the comparisons in Figure 12, suggest that the S cluster has not yet completely relaxed in either a resonant or nonresonant way. Short-period S-cluster members could have been influenced by vector resonant relaxation, which changed their orbital inclination, especially for more peaked stellar-density distributions with $\gamma_s \sim 1.0$; see Figure 12. However, because of the young age of S stars comparable to CW-disk stars, vector resonant relaxation is not expected to lead to the complete randomization of stellar inclinations for S stars with larger semimajor axes (longer periods) as has been previously argued to explain the apparent nearly isotropic S-cluster distribution (Genzel et al. 2010), which is not confirmed in this work. Scalar resonant relaxation, which influences orbital eccentricities and semimajor axes of stars, takes place on timescales at least one order of magnitude longer than the age of S stars.

Hence, the S cluster can in principle keep the nonisotropic structure, consisting of two inclined disks embedded within the outer CW disk. This may be hypothesized to originate in the way the S cluster formed. In particular, the S stars were likely formed within the infalling cloud/streamer that formed the disk around Sgr A* upon its impact, as seems to be the case for OB stars that are a part of the CW disk farther out (Levin & Beloborodov 2003). Due to its age of several million years, the S cluster is expected to keep the imprints of the original formation mechanism within the gas/stellar disk, which potentially consisted of more inclined streamers. The coexistence of more inclined gaseous disks is also predicted by hydrodynamical simulations of star formation in the Galactic center within an infalling massive molecular cloud. The multiple inclined disks may result from an infall of a massive molecular cloud or from a cloud–cloud collision (Hobbs & Nayakshin 2009; Alig et al. 2013; Lucas et al. 2013).

(b) *Kozai–Lidov oscillations due to a massive disk*

In addition, the current S-cluster distribution can reflect the perturbation by an outer massive stellar or gas disk in the distance range of 0.04–0.5 pc, which led to Kozai–Lidov-type resonances, i.e., to the interchange between the orbital eccentricity and inclination because of the conservation of the z component of the angular momentum, $L_z = \sqrt{(1 - e^2)} \cos i = \text{const.}$

The Kozai–Lidov process can be induced by a rather massive gaseous disk present in the past. Concerning the gas disk, in Figure 12 we can see that this would be the case for a

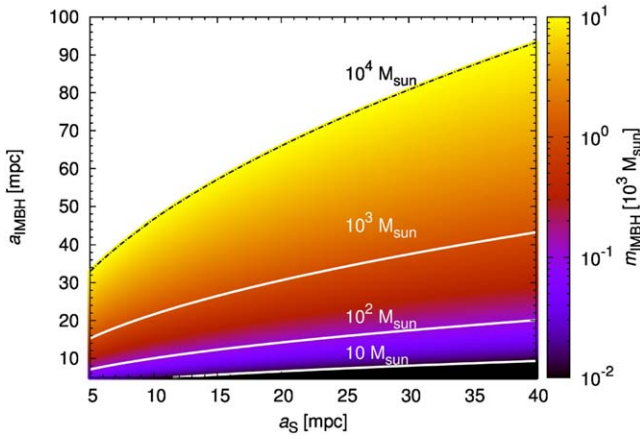


Figure 13. The color-coded mass of the IMBH as a function of its semimajor axis (circular orbit) and the semimajor axis of S stars for which the timescale of Kozai–Lidov oscillations is 1.9 Myr (lower limit on the age of S stars).

very massive disk of $M_r = 10^8 M_\odot$ positioned at $r = 0.4$ pc (outer boundary of the CW disk). The same Kozai timescale is obtained for a less massive disk of $M_r = 10^5 M_\odot$ that is closer, at $r = 0.04$ pc (inner boundary of the CW disk), i.e., one order of magnitude closer to the black hole. Such a scenario with a massive gaseous disk that extended to smaller radii in the past than the current stellar disk was studied by Chen & Amoroso-Seoane (2014). In their study, the Kozai–Lidov resonance induced by the disk could explain the current, thermalized distribution of mostly B-type S stars as well as the presence of more massive OB stars outside the S cluster. In their Figure 1, the estimate of the age of the DSO/G2 NIR-excess object is $\sim 10^5$ – $10^{5.5}$ yr, consistent with the pre-main-sequence star as studied by Zajaček et al. (2017).

(c) *Kozai–Lidov oscillations due to a massive perturber (IMBH)*

Alternatively, the Kozai–Lidov oscillation on the timescale of the order of 1 Myr can develop due to the presence of a massive body–perturber in the inner parsec, in particular the IMBH of mass M_{IMBH} with the semimajor axis of a_{IMBH} and the eccentricity e_{IMBH} . Any S-star then behaves as a test body that orbits Sgr A* and is perturbed by an IMBH farther out. The period of the oscillation is (Naoz 2016)

$$T_{\text{KL}}^{\text{IMBH}} = 2\pi \frac{\sqrt{GM_*}}{Gm_{\text{IMBH}}} \frac{a_{\text{IMBH}}^3}{a_*^{3/2}} (1 - e_{\text{IMBH}}^2)^{3/2}. \quad (8)$$

To get the specific estimates of the mass of the IMBH and its location with respect to the S cluster, we assume the IMBH orbits Sgr A* on a circular orbit and hence $e_{\text{IMBH}} = 0$. In Figure 13, we show how the location of the IMBH with respect to the S cluster depends on its mass (in the range 10 – $10^4 M_\odot$) in order to induce Kozai–Lidov oscillation in the inclination and the eccentricity during the lifetime of the S cluster. We assumed $T_{\text{KL}} = 1.9$ Myr. We see that IMBHs with mass of $m_{\text{IMBH}} = 10^3 M_\odot$ and lower would essentially have to orbit Sgr A* within the S cluster on a circular orbit. Only those with $m_{\text{IMBH}} = 10^4 M_\odot$ and heavier could also be located outside the inner arcsecond to induce the Kozai–Lidov resonance in short enough time for S-cluster members.

From Equation (8), it is apparent that the Kozai–Lidov timescale can significantly shorten for perturbers–IMBHs that orbit Sgr A* on a highly eccentric orbit, which can originate due to dynamical scattering in the nuclear star cluster.

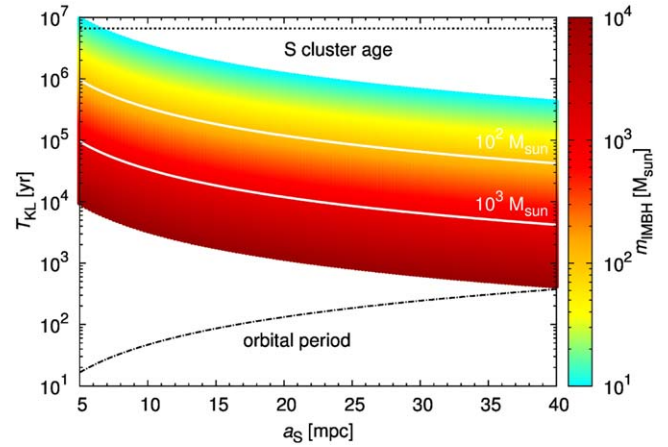


Figure 14. The color-coded mass of the IMBH as a function of the Kozai–Lidov timescale and of the semimajor axis of S stars. The IMBH is assumed to have a semimajor axis of 0.04 pc and its orbit is highly eccentric, $e = 0.99$.

Specifically, for the IMBH semimajor axis of $a = 0.04$ pc (approximately S cluster length-scale) and the eccentricity of $e_{\text{IMBH}} = 0.99$, even stellar black holes of mass of the order of $m_{\text{IMBH}} = 10 M_\odot$ could induce Kozai–Lidov oscillation within the S-cluster lifetime; see Figure 14. For heavier IMBHs, the Kozai–Lidov timescale shortens as $T_{\text{KL}} \propto m_{\text{IMBH}}^{-1}$.

In conclusion, a massive perturber within or just outside the S cluster can induce the eccentricity–inclination Kozai–Lidov oscillations within the S-cluster lifetime, i.e., an initially disk-like stellar system can get misaligned or an initially spherical system can become nonisotropic with respect to the inclination distribution, especially due to Kozai–Lidov dependency on initial inclinations—it applies most significantly to highly inclined stellar orbits with respect to the perturber, $i \sim 40^\circ$ – 140° . Once the system is perturbed due to the Kozai–Lidov resonance, it would take at least $T_{\text{RR},v} \approx 10^6$ yr for vector resonant relaxation to randomize orbits. Hence, the current S-cluster state can reflect a recent perturbation due to the presence of an IMBH. Although detailed dynamical modeling is beyond the scope of this paper, the analysis of Tisserand’s parameter can give limited insight into the action of a massive perturber near the S cluster surrounding Sgr A*.

(d) *Tisserand’s parameter*

Tisserand’s parameter is a dynamical quantity that is used to describe restricted three-body problems in which the three objects all differ greatly in mass. Tisserand’s parameter is calculated from several orbital elements (semimajor axis a , orbital eccentricity e , and inclination i_b) of a small object and a larger perturbing body, all of which are in orbit about a greater central mass. This parameter is a dynamically useful quantity as it is approximately conserved during an encounter of the two smaller bodies. It therefore allows us to connect the post-encounter dynamical properties with the pre-encounter properties (Merritt 2013). In the following, we see that the analysis of Tisserand’s parameter for the S-cluster stars suggests that two perpendicular disks can be supported by a heavy mass just outside the S cluster, influencing its dynamics.

Tisserand’s parameter can be written as

$$T = \frac{a_{\text{Pert}}}{2a} + \left[\frac{a}{a_{\text{Pert}}} (1 - e^2) \right]^{1/2} \cos(i_b). \quad (9)$$

The ratio between the semimajor axes of a massive perturber and the stars is $R' = a_{\text{Pert}}/a$. Assuming the stars are in a disk

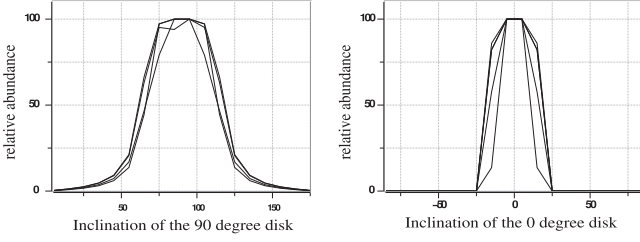


Figure 15. The peak normalized distributions of inclinations i_{obs} that can be derived from $i_b = 90^\circ$ (left) and $i_b = 0^\circ$ (right) via Tisserand’s parameter using the observed distribution of eccentricities.

and had semimajor axes $a = a_{\text{Pert}}/R'$ and an eccentricity e close to zero, then $T = R'/2 + R'^{-1/2}$. Then, T or $\mu = R' + 2R'^{-1/2}$, respectively, describe the initial setup. For $R' = 1$, one finds $T = 3/2$ and $\mu = 3$. For the current orbital elements (a , e , i_b) and the current ratio $R = a_{\text{Pert}}/a$, one can write Tisserand’s relation for each star as

$$R + 2[R^{-1}(1 - e^2)]^{1/2} \cos(i_b) \approx \mu. \quad (10)$$

Here, i_b is the inclination of the stars with respect to the plane in which the massive perturber orbits the central mass and $R = a_{\text{Pert}}/a$ is the current ratio between the semimajor axes of a massive perturber and the stars. This expression can be rewritten as

$$\cos(i_b) = \pm \sqrt{\frac{R(\mu - R)^2}{4(1 - e^2)}}. \quad (11)$$

This relation has simple solutions for cases in which $\mu \sim R$ with μ now containing information on the initial conditions R' . For $R'/R > 1.0$, one can reproduce the $i_b = 90^\circ$ disk and for $R'/R < 1.0$ one can reproduce the $i_b = 0^\circ$ disk. If one allows the current ratio R to vary by a few percent and uses the distribution of observed eccentricities as an input, one can reproduce the distribution of observed stellar inclinations for the $i_b = 90^\circ$ disk. Compared to the $i_b = 90^\circ$ disk, the inclination distribution for the $i_b = 0^\circ$ disk turns out to be narrower. Both distributions are shown in Figure 15. On the sky, we observe both disks such that their inclinations toward the observer are both close to the observed inclination $i_{\text{obs}} = 90^\circ$; hence, the two distributions are superimposed if derived from observations of the central arcsecond in total.

Solving Equation (11) for increasing values of R' , one finds that the value for the current ratio R approximates that for initial ratio R' . In Figure 16, we plot the current ratio R in relation to R' . The top graph shows how R/R' approximates unity for the $i_b = 90^\circ$ disk as listed in Table 1. The bottom graph shows the same for the $i_b = 0^\circ$ disk. For values $R' \geq 6 \dots 8$, the difference between the two ratios drops so that R/R' gets close to unity to within less than about three to five times the width by which we need to let R vary to explain the observed distributions of inclinations (see Figure 16). This means that for these cases, the initial conditions are very similar to the current conditions and the two orthogonal disks may be populated by objects with rather similar dynamical properties. Hence, we find as a result the analysis of Tisserand’s parameter that two perpendicular disks can be supported by a heavy mass just outside the S cluster, influencing its dynamics. This fits well with IRS 13E being a possible disturber of the S-cluster star. A discussion is given in Section 3.2.2.

Under the influence of a massive perturber, the eccentricity and inclination of the stars may vary periodically with the stars’

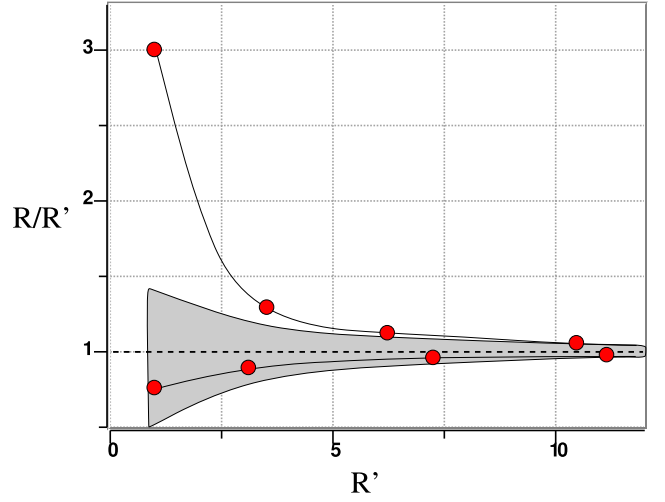


Figure 16. The current ratio R in relation to the initial ratio R/R' as a function of the initial ratio R' . The gray areas shows the range covered by three times the actual range by which the current ratio R is allowed to carry in order to explain the distribution of inclinations.

argument of periastris ω under conservation of $(1 - e^2)\cos(i)$. The timescale for these “Kozai–Lidov cycles” is of the order of 10^6 yr for the S stars within the central $1''$ – $3''$ if the mass of the perturber is of the order of 10^3 – $10^4 M_\odot$ (see text and Equation 8.175 in Merritt 2013). However, there is no specific timescale associated with Tisserand’s parameter and the formation or conservation of the system. If at the time of the formation of the stellar disk the stars had the observed configuration, then they will all satisfy Equation (11) from the start and at all later times, until some other perturbation acts. Stars that are on orbits that do not satisfy the relation will be removed or associated with one of the disks on a few Lidov–Kozai timescales or the resonant relaxation timescales (see above). Two orthogonal disks will be supported by Tisserand’s relation and the interrelation of stellar angular momenta as described by Equation (11).

3.2.2. Possible Sources of Perturbation

The strong vertical resonances expressing themselves via the X-shaped structure in the stellar distribution can be the result of a resonant relaxation process solely determined by the mean field of stars in the cluster. Furthermore, the growth of the Galactic bar could trigger inner Lindblad resonances, in which the stars are lifted into higher-amplitude orbits (Quillen 2002; Binney & Tremaine 2008). However, one may identify possible sources of perturbation that imposed these resonances or influenced the relaxation process.

Possibility 1: The B stars of the S cluster are estimated to have an age less than 15 Myr. However, star S2 has an age of about 7 Myr, which is compatible with the age of the CWD of young stars in the GC. It is quite likely that S stars formed almost simultaneously with the OB/WR stars that are part of the CW disk (Habibi et al. 2017). It is thought that the CW-disk stars formed in situ in a massive gaseous disk (Levin & Beloborodov 2003). The origin of this disk could have been a massive molecular cloud with the radius of ~ 15 pc and the impact parameter of ~ 26 pc, which was tidally disrupted, spiraled in, and subsequently formed an eccentric disk (Mapelli et al. 2012) where stars formed. It cannot be excluded that the stellar disk, which previously extended below 0.04 pc where the S cluster is located now, was perturbed by the infall of

another massive molecular cloud that formed a disk or a ring with an inclination of β with respect to the stellar disk (Mapelli et al. 2013; Trani et al. 2016). The influx of gas that led to their formation also induced the perturbances in the young S cluster, resulting in vertical resonances that relaxed to the structure seen today. According to the numerical simulations of Mapelli et al. (2013) and Trani et al. (2016), the precession driven by the gas disk in the inner 0.5 pc on the stellar disk can significantly increase the stellar inclinations within a few million years, which leads to the disk tilting and/or warping. As the precession is faster for outer disk parts, $T_{\text{prec}} \propto a_*^{-3/2}$, the S cluster could in principle represent a “primordial” disk part with two perpendicular streamers that have warped to form the CW disk at larger distances. Further warping at largest distances led to disk dismembering, which can account for $\sim 80\%$ of OB stars that are not part of any disk (Yelda et al. 2014). Two innermost, nearly perpendicular stellar disks are in a dynamically very stable configuration, because the mutual disk precession $T_{\text{DISC}} \propto \cos \beta^{-1}$ around each other goes to infinity for the inclination β that approaches 90° .

Possibility 2: As the orbits are clearly not fully randomized, a massive IMBH within the S cluster can probably be excluded (see comments in the introduction and see Gualandris & Merritt 2009). However, an IMBH as a massive perturber well outside the S cluster could provide a long-term influence on the orbits resulting in vertical resonances. The analysis of the Kozai–Lidov oscillations and Tisserand’s parameter both suggests that a massive perturber may have influenced the stellar dynamics in the central arcsecond. For an initial ratio of the semimajor axes of the stars and the perturber of $R' \geq 6 \dots 8$, the ratio between the initial and current ratio becomes unity. In this case, the dynamical situation may not have changed very much since the system was set up. Assuming that the semimajor axes a of the stars can be taken as a measure of the radius of the S-star cluster, i.e., $a = 0''.5$, then $R' \sim R \sim 3''.5$ (0.13 pc projected distance). This fits well with the separation of IRS 13E from Sgr A* and the S-cluster star. IRS 13E lies within $\sim 15^\circ$ in one of the stellar disks. It may harbor an up to $10^4 M_\odot$ IMBH and a few hundred solar masses of stars (Krabbe et al. 1995; Maillard et al. 2004; Schödel et al. 2005; Tsuboi et al. 2017). The analysis of the Kozai–Lidov oscillations and Tisserand’s parameter then indicate that the 0° – 90° disk in Section 3.2.1(d) can to first order be identified as the red and black disk as discussed in Sections 3.1.3 and 3.1.2.

The possibility of different coexisting stellar disks in the GC has also been discussed theoretically by Mastrobuono-Battisti et al. (2019). Here, the authors simulate multiple stellar disks in the central stellar cluster. Each disk is added after 100 Myr. In particular, in the bottom panel of their Figure 1, one can see that even after 100 Myr two separate stellar disks can still be distinguished. The first one got thicker but is still well defined.

4. Summary and Conclusions

We present a detailed analysis of the kinematics of the stars in the innermost stellar cluster for which we have orbital elements. The high-velocity S-cluster stars orbit the SMBH Sgr A* at the center of the MW. The distribution of inclinations and position angles of the sky-projected orbits deviate significantly from a uniform distribution which one would have expected if the orientation of the orbits are random. The stars are arranged in two stellar disks that are perpendicular to each other and located within a position angle of about $\pm 45^\circ$ with respect to

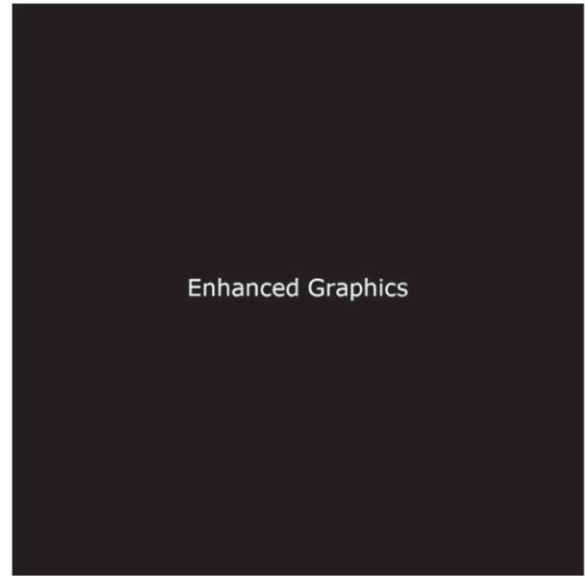


Figure 17. Animation of the projected orbital arrangements in motion. There are three sequences in the animation: the full three-dimensional orbits using all orbital elements, a sequence where the ellipticity has been set to zero, and a normalized sequence where the semimajor axes have been set to a constant and the ellipticity has been set to zero.

(An animation of this figure is available.)

the Galactic plane. The distribution of eccentricities of the inner (black) north–south disk system suggests that it is relaxed and thermal as it may be expected from the Hills mechanism. The east–west (red) disk system is more influenced by a disk-migration scenario as it approaches the less-than-thermal side in the distribution of the eccentricities.

While it cannot be excluded that the red disk is the inner part of the CWD of He stars (Levin & Beloborodov 2003; Paumard et al. 2006) or is connected to it, the black disk system is much more compact and possibly more thermally relaxed. It is uncertain if or how it is connected to the large central cluster.

Because the angular momentum vectors of the stars in each disk point in opposite directions, i.e., the stars in a given disk rotate both ways, it appears to be unlikely that the origin or history of these stars is the same as the one discussed for the massive young stellar disks containing the He stars (Levin & Beloborodov 2003; Paumard et al. 2006; Lu et al. 2009, 2013; Yelda et al. 2014). Most likely, the S-cluster structure is strongly influenced by the Kozai–Lidov resonances or vector resonant relaxations.

This prominent X-shaped arrangement is most likely a result of the interaction of stars with each other that can be described via the resonant relaxation process. An estimate of the resonant relaxation timescale indicates that the structure started to evolve into the current X shape in the same time interval during which most of the young stars in the central stellar cluster were formed. The presence of a highly ordered kinematic structure at the center of the nuclear stellar cluster and in the immediate vicinity of the SMBH Sgr A* also indicates that for a very long time, no major perturbation of the system occurred that could have led to a randomization of the stellar orbits in the central arcsecond.

5. Enhanced Graphics

Figure 17 provides three animations where the SMBH Sgr A* is located at the center of the three-dimensional arrangement.

The animations hold for a short while at the positions under which the orbital configuration can be seen in special projections: red system face on, line-of-sight view, pole vision, and red system edge on. Labels in units of milliparsecs are given at the edges. In each animation, we list the corresponding azimuth and elevation angle, with 0° and -90° , respectively, being the line-of-sight direction. In the first sequence, we show the full three-dimensional orbits using all orbital elements. The dots on the orbits indicate the position of the star. The corresponding time is given in a text line above. In the second sequence, the ellipticity has been set to zero. Finally, we show the ball of wool configuration. Here, semimajor axes have been set to a constant and the ellipticity has been set to zero.

We are grateful to Anna Luka Höfling, who prepared the enhanced graphics as an intern in the infrared group at the I. Physikalisches Institut of the University of Cologne. We received funding from the European Union Seventh Framework Program (FP7/2007-2013) under grant agreement No. 312789—Strong gravity: Probing Strong Gravity by Black Holes Across the Range of Masses. This work was supported in part by the Deutsche Forschungsgemeinschaft (DFG) via the Cologne Bonn Graduate School (BCGS), the Max Planck Society through the International Max Planck Research School (IMPRS) for Astronomy and Astrophysics, as well as special funds through the University of Cologne and CRC 956—Conditions and Impact of Star Formation under project A2. M. Z. acknowledges the financial support by the National Science Centre, Poland, grant No. 2017/26/A/ST9/00756 (Maestro 9). We thank the German Academic Exchange Service (DAAD) for support under COPRAG2015 (No.57147386) and the the Czech Science Foundation—DFG collaboration (EC 137/10-1).

Appendix A Field-of-view Effects

By restricting the field of view toward a central section with radius $\Delta s \sim 0.5$ covering the surface $4(\Delta s)^2$ in the sky, one introduces a bias toward higher inclinations. Sources with low inclinations with orbits outside the selected area and sources with large three-dimensional distances from the center pass through the selected area only if their orbits have high inclinations. We assume that the central volume is $16(\Delta s)^3$ and the volume attributed to the outer stars within the column $4(\Delta s)^2$ is $8(\Delta s)^2$. The central arcsecond is dominated by young stars. Early-type stars are abundant within the central $5''$ radius (i.e., $10\Delta s$) of the nuclear cluster with a surface (volume) density dropping with an exponent of -1.8 (-2.8 ; Buchholz et al. 2009). Taking the volume density at $3''$ – $4''$ radius, i.e., at 6 to 8 times Δs , then the number ratio of stars between those that are within the volume of the central arcsecond and those that are only in projection in that region is

$$\left(\frac{\Delta s}{(6 \dots 8)\Delta s} \right)^{-2.8} \frac{16(\Delta s)^3}{8(\Delta s)^2 10\Delta s} = (30 \dots 67). \quad (\text{A1})$$

Hence, the bias is only of the order of a few percent and the clustering toward 90° inclination can be fully attributed to the intrinsic properties of the stellar orbits.

In summary, these findings indicate that independent of the three-dimensional orientation, the determined stellar orbits in the S cluster are preferentially seen edge on.

Appendix B Biases Due to Incomplete Orbital Coverage

O’Neil et al. (2019) discuss the influence of orbital elements resulting from fits to data that only cover the orbits in an incomplete way. They introduce an observable-based prior (OBP) paradigm and the corresponding bias factors with respect to uniform priors (UP). In our case, the orbital coverage of the fitted orbits indicates three groups.

The first group, which contains stars with 40%–100% orbital coverage, has no difference between the bias factor of uniform priors UP and the bias factor of the OBP for the black hole mass and the distance to the GC. The second group, which contains stars with 20%–35% orbital coverage, has a difference of 0.3σ between the bias factor of UP [0.5σ – 0.8σ] and the bias factor of OBP [0.2σ – 0.5σ] for the case of the SMBH mass and the distance to it. The last group, which contains stars with 5%–15% orbital coverage, has a difference of [0.51σ – 0.6σ] between the bias factor of UP [0.98 – 1] and the bias factor of OBP [0.4σ – 0.47σ] for the case of SMBH mass and the distance to it. The bias factor difference for the orbital elements (O’Neil et al. 2019) was only done for the case of 16% orbital coverage, i.e., valid only for the last group. Here, a value of 1 indicates high bias and a value of -1 is low bias (see O’Neil et al. 2019).

In summary, the inclination bias factor difference is extremely small. For 19 stars only, we find a 0.6σ difference. Hence, our finding that the stars are preferentially on highly inclined orbits is unaffected by this bias. Also, the orbital elements we derive for the stars are only affected in a minimal way.

ORCID iDs

Basel Ali  <https://orcid.org/0000-0002-5728-4054>
 Andreas Eckart  <https://orcid.org/0000-0001-6049-3132>
 Michal Zajacek  <https://orcid.org/0000-0001-6450-1187>
 Florian Peißker  <https://orcid.org/0000-0002-9850-2708>
 Gunther Witzel  <https://orcid.org/0000-0003-2618-797X>

References

- Abbott, C. G., Valluri, M., Shen, J., & Debattista, V. P. 2017, *MNRAS*, **470**, 1526
 Ajne, B. 1968, *Biometrika*, **55**, 343
 Alig, C., Scharmann, M., Burkert, A., & Dolag, K. 2013, *ApJ*, **771**, 119
 Antonini, F., Capuzzo-Dolcetta, R., Mastrobuono-Battisti, A., & Merritt, D. 2012, *ApJ*, **750**, 111
 Bhattacharyya, G., & Johnson, R. 1969, *Biometrika*, **56**, 446
 Binney, J., & Tremaine, S. 2008, in *Galactic Dynamics*, ed. J. Binney & S. Tremaine (2nd ed.; Princeton, NJ: Princeton Univ. Press), 539
 Boehle, A., Ghez, A. M., Schödel, R., et al. 2016, *ApJ*, **830**, 17
 Buchholz, R. M., Schödel, R., & Eckart, A. 2009, *A&A*, **499**, 483
 Chaves-Velasquez, L., Patsis, P. A., Puerari, I., Skokos, C., & Manos, T. 2017, *ApJ*, **850**, 145
 Chen, X., & Amaro-Seoane, P. 2014, *ApJL*, **786**, L14
 Contopoulos, G. 1988, *A&A*, **201**, 44
 Durand, D., & Arthur, G. J. 1958, *JG*, **66**, 229
 Eckart, A., Mužić, K., Yazici, S., et al. 2013, *A&A*, **551**, A18
 Genzel, R., Eisenhauer, F., & Gillessen, S. 2010, *RvMP*, **82**, 3121
 Gerhard, O., Wegg, C., & Portail, M. 2016, in *The Universe of Digital Sky Surveys*, ed. N. R. Napolitano (Cham: Springer), 41
 Ghez, A. M., Duchêne, G., Matthews, K., et al. 2003, *ApJL*, **586**, L127
 Gilbert, G. 1895, *Bull. Phil. Soc. Washington*, **12**, 241
 Gillessen, S., Eisenhauer, F., Trippe, S., et al. 2009, *ApJ*, **692**, 1075
 Gillessen, S., Genzel, R., Fritz, T. K., et al. 2012, *Natur*, **481**, 51
 Gillessen, S., Plewa, P. M., Eisenhauer, F., et al. 2017, *ApJ*, **837**, 30
 Gravity Collaboration, Abuter, R., Amorim, A., et al. 2018, *A&A*, **615**, L15
 Gualandris, A., & Merritt, D. 2009, *ApJ*, **705**, 361
 Habibi, M., Gillessen, S., Martins, F., et al. 2017, *ApJ*, **847**, 120

- Hernquist, L., & Weinberg, M. D. 1992, [ApJ](#), **400**, 80
- Hills, J. G. 1988, [Natur](#), **331**, 687
- Hobbs, A., & Nayakshin, S. 2009, [MNRAS](#), **394**, 191
- Hopman, C., & Alexander, T. 2006, [ApJ](#), **645**, 1152
- Jalali, B., Pelupessy, F. I., Eckart, A., et al. 2014, [MNRAS](#), **444**, 1205
- Jammalamadaka, S. R., & SenGupta, A. 2001, *Topics in Circular Statistics* (Singapore: World Scientific)
- Krabbe, A., Genzel, R., Eckart, A., et al. 1995, [ApJL](#), **447**, L95
- Levin, Y., & Beloborodov, A. M. 2003, [ApJL](#), **590**, L33
- Lu, J. R., Do, T., Ghez, A. M., et al. 2013, [ApJ](#), **764**, 155
- Lu, J. R., Ghez, A. M., Hornstein, S. D., et al. 2009, [ApJ](#), **690**, 1463
- Lucas, W. E., Bonnell, I. A., Davies, M. B., & Rice, W. K. M. 2013, [MNRAS](#), **433**, 353
- Maillard, J. P., Paumard, T., Stolovy, S. R., & Rigaut, F. 2004, [A&A](#), **423**, 155
- Mapelli, M., Gualandris, A., & Hayfield, T. 2013, [MNRAS](#), **436**, 3809
- Mapelli, M., Hayfield, T., Mayer, L., & Wadsley, J. 2012, [ApJ](#), **749**, 168
- Martins, F., Gillessen, S., Eisenhauer, F., et al. 2008, [ApJL](#), **672**, L119
- Mastrobuono-Battisti, A., Perets, H. B., Gualandris, A., Neumayer, N., & Sippel, A. C. 2019, [MNRAS](#), **490**, 5820
- Menten, K. M., Reid, M. J., Eckart, A., & Genzel, R. 1997, [ApJL](#), **475**, L111
- Merritt, D. 2013, *Dynamics and Evolution of Galactic Nuclei* (Princeton, NJ: Princeton Univ. Press)
- Naoz, S. 2016, [ARA&A](#), **54**, 441
- O’Neil, K. K., Martinez, G. D., Hees, A., et al. 2019, [AJ](#), **158**, 4
- Parsa, M., Eckart, A., Shahzamanian, B., et al. 2017, [ApJ](#), **845**, 22
- Paumard, T., Genzel, R., Martins, F., et al. 2006, [ApJ](#), **643**, 1011
- Peißker, F., Eckart, A., & Parsa, M. 2020, [ApJ](#), **889**, 61
- Plewa, P. M., Gillessen, S., Eisenhauer, F., et al. 2015, [MNRAS](#), **453**, 3234
- Quillen, A. 2002, [AJ](#), **124**, 400
- Quillen, A. C., Kuchinski, L. E., Frogel, J. A., & DePoy, D. L. 1997, [ApJ](#), **481**, 179
- Quillen, A. C., Minchev, I., Sharma, S., Qin, Y.-J., & Di Matteo, P. 2014, [MNRAS](#), **437**, 1284
- Rauch, K. P., & Tremaine, S. 1996, [NewA](#), **1**, 149
- Reid, M. J., Menten, K. M., Genzel, R., et al. 2003, [ApJ](#), **587**, 208
- Reid, M. J., Menten, K. M., Trippe, S., Ott, T., & Genzel, R. 2007, [ApJ](#), **659**, 378
- Sabha, N., Eckart, A., Merritt, D., et al. 2012, [A&A](#), **545**, A70
- Schödel, R., Eckart, A., Iserlohe, C., Genzel, R., & Ott, T. 2005, [ApJL](#), **625**, L111
- Schödel, R., Merritt, D., & Eckart, A. 2009, [A&A](#), **502**, 91
- Shahzamanian, B., Eckart, A., Valencia-S., M., et al. 2015, [A&A](#), **576**, A20
- Stephan, A. P., Naoz, S., Ghez, A. M., et al. 2016, [MNRAS](#), **460**, 3494
- Šubr, L., & Karas, V. 2005, [A&A](#), **433**, 405
- Trani, A. A., Mapelli, M., Bressan, A., et al. 2016, [ApJ](#), **818**, 29
- Tsuboi, M., Kitamura, Y., Tsutsumi, T., et al. 2017, [ApJL](#), **850**, L5
- Valencia-S., M., Eckart, A., Zajaček, M., et al. 2015, [ApJ](#), **800**, 125
- Witzel, G., Eckart, A., Bremer, M., et al. 2012, [ApJS](#), **203**, 18
- Witzel, G., Ghez, A. M., Morris, M. R., et al. 2014, [ApJL](#), **796**, L8
- Yelda, S., Ghez, A. M., Lu, J. R., et al. 2014, [ApJ](#), **783**, 131
- Yusef-Zadeh, F., Royster, M., Wardle, M., et al. 2013, [ApJL](#), **767**, L32
- Yusef-Zadeh, F., Wardle, M., Kunneriath, D., et al. 2017, [ApJL](#), **850**, L30
- Zajaček, M., Britzen, S., Eckart, A., et al. 2017, [A&A](#), **602**, A121